Assessment of NASA GISS CMIP5 and Post-CMIP5 Simulated Clouds and TOA Radiation Budgets Using Satellite Observations. Part II: TOA Radiation Budget and CREs

RYAN E. STANFIELD, XIQUAN DONG, AND BAIKE XI

Department of Atmospheric Sciences, University of North Dakota, Grand Forks, North Dakota

ANTHONY D. DEL GENIO

NASA Goddard Institute for Space Studies, New York, New York

PATRICK MINNIS, DAVID DOELLING, AND NORMAN LOEB

NASA Langley Research Center, Hampton, Virginia

(Manuscript received 25 March 2014, in final form 19 November 2014)

ABSTRACT

In Part I of this study, the NASA GISS Coupled Model Intercomparison Project (CMIP5) and post-CMIP5 (herein called C5 and P5, respectively) simulated cloud properties were assessed utilizing multiple satellite observations, with a particular focus on the southern midlatitudes (SMLs). This study applies the knowledge gained from Part I of this series to evaluate the modeled TOA radiation budgets and cloud radiative effects (CREs) globally using CERES EBAF (CE) satellite observations and the impact of regional cloud properties and water vapor on the TOA radiation budgets. Comparisons revealed that the P5- and C5-simulated global means of clear-sky and all-sky outgoing longwave radiation (OLR) match well with CE observations, while biases are observed regionally. Negative biases are found in both P5- and C5-simulated clear-sky OLR. P5-simulated all-sky albedo slightly increased over the SMLs due to the increase in low-level cloud fraction from the new planetary boundary layer (PBL) scheme. Shortwave, longwave, and net CRE are quantitatively analyzed as well. Regions of strong large-scale atmospheric upwelling/downwelling motion are also defined to compare regional differences across multiple cloud and radiative variables. In general, the P5 and C5 simulations agree with the observations better over the downwelling regime than over the upwelling regime. Comparing the results herein with the cloud property comparisons presented in Part I, the modeled TOA radiation budgets and CREs agree well with the CE observations. These results, combined with results in Part I, have quantitatively estimated how much improvement is found in the P5-simulated cloud and radiative properties, particularly over the SMLs and tropics, due to the implementation of the new PBL and convection schemes.

1. Introduction

Although many improvements have been made to the global circulation models (GCMs) involved in the Coupled Model Intercomparison Project phase 5 (CMIP5) project (Lauer and Hamilton 2013; Jiang et al. 2012; Wang and Su 2013, Li et al. 2013; Klein et al. 2013; Chen et al. 2013; Stanfield et al. 2014; Dolinar et al. 2014), clouds and their radiative feedbacks are still a problem in climate models as concluded by the Intergovernmental Panel on Climate Change (IPCC) in their Fifth Assessment Report (AR5; see chapter 9 therein; Flato et al. 2013). Lauer and Hamilton (2013) have revealed that the model simulated cloud radiative effects (CREs) tend to outperform cloud fractions (CFs), suggesting that models are not accurately depicting fundamental cloud processes; rather, the models are being tuned to provide simulations closer to observations. Jiang et al. (2012) developed a grading scale in an attempt to rate each model based upon spatial mean, standard deviation, and correlation and highlighted that there exists large model spread and a high degree of discrepancy from observations, particularly in the upper

Corresponding author address: Dr. Xiquan Dong, Department of Atmospheric Sciences, University of North Dakota, 4149 University Ave. Stop 9006, Grand Forks, ND 58202-9006.
E-mail: dong@aero.und.edu

DOI: 10.1175/JCLI-D-14-00249.1

© 2015 American Meteorological Society

troposphere. Dolinar et al. (2014) evaluated 28 CMIP5 AMIP GCMs' simulated clouds and the top of the atmosphere (TOA) radiation budget and concluded that the multimodel ensemble mean CF (57.6%) is, on average, underestimated by 7.6% when compared to Clouds and the Earth's Radiant Energy System–Moderate Resolution Imaging Spectroradiometer (CERES-MODIS, herein CM) results between 65°S and 65°N, although, there are good agreements in the TOA radiation budget.

In the first paper of this series (Stanfield et al. 2014, hereafter Part I), we investigated the cloud properties simulated by the National Aeronautics and Space Administration (NASA) GISS-E2 atmospheric GCM [post-CMIP5 (P5)] and its CMIP5 (C5) predecessor in comparison against multiple satellite observations including CERES-MODIS, *CloudSat*/*CALIPSO* (CC), the Atmospheric Infrared Sounder (AIRS), and the Advanced Microwave Sounding Radiometer for Earth Observing System (AMSR-E), as clouds and cloud feedbacks have long been one of the largest sources of uncertainty in predicting future climate change (Cess et al. 1989; Wielicki et al. 1995; Houghton et al. 2001; Stephens 2005; Bony et al. 2006; Randall et al. 2007). Although some improvements have been made in the P5 simulation on a global scale, the largest improvements have been found over the southern midlatitudes (SMLs), where the correlations to observations have increased and bias and RMSE have significantly decreased compared to the previous C5 simulations. Changes to the planetary boundary layer (PBL) scheme implemented in the GISS P5 GCM have resulted in improved total CFs, particularly over the SMLs where marine boundary layer (MBL) CFs have increased by ~20% relative to the previous C5 simulation, bringing the P5 total column CF closer to observations. P5-simulated cloud water paths (CWPs), however, are 25 g m^{-2} lower than C5 results. As discussed in Part I, while these results bring the P5 simulations closer to observations, this small change may be an artifact given that the CWP diagnostic in the GCM is for stratiform clouds only. P5 has more frequent shallow convection than C5 in the SMLs (Fig. 7 of Yao and Cheng 2012), causing an apparent decrease since its cloud water is not accounted for in CWP. The P5-simulated precipitable water vapor (PWV) and relative humidity (RH) agree well with both the AMSR-E and AIRS observations, with an atmosphere moister and wetter than the previous C5 results. The moister and wetter atmospheric conditions simulated by P5 are consistent with our CF comparison and provide strong support for the increased MBL clouds over the SMLs. Over the tropics, the P5-simulated total CFs and CWPs are slightly lower than the C5 results, bringing the model results closer to observations, primarily due to the shallower tropical boundary layer in P5 relative to C5 in regions outside the marine stratocumulus decks.

Based on the findings of Part I, here in Part II we investigate how the improved cloud properties in the P5 simulation can impact the TOA radiation budget and cloud radiative effects. Specifically, this study compares the P5- and C5-simulated clear-sky and all-sky outgoing longwave (LW) radiation (OLR) and albedos at TOA, as well as their cloud radiative effects with CERES EBAF (CE) results. While most GCMs simulate the global TOA radiation budget well, it is necessary to assess the regional changes to the radiation budget associated with the two new schemes in the P5 simulation, particularly over the SMLs and the tropics.

Section 2 briefly describes the changes made to the C5 version of the model to generate the P5 simulation. These changes are more thoroughly described in Part I. The NASA CERES EBAF satellite data product, the methodology in generating global means, and our method for the calculations of CRE are also described in section 2. Section 3 compares the results globally of both model runs with satellite observations and quantitatively estimates the improvement found in the P5 simulation. Section 4 examines the impact of cloud properties and PWV on all-sky OLR and albedo at TOA over two significantly different dynamic regimes: regions of strong atmospheric upwelling and downwelling over the oceans. Section 4 also contains a quantitative estimate of improvements over the SMLs in the new P5 simulation. The results are summarized in section 5. Because the number of acronyms used in this study is quite large, many acronyms used in this study are listed and defined in Table 1.

2. Datasets and methodology

a. GISS-E2 CMIP5 and post-CMIP5 model runs

This study uses two versions of the NASA GISS E2 model. The monthly CMIP5 AMIP r5i1p3 ensemble member of the GISS-E2 model with prescribed sea surface temperatures (SSTs) was retrieved using the ESGF PCMDI database (Taylor et al. 2012). The P5 intermediate diagnostic data are provided by NASA GISS and incorporate two major parameterization changes. The cumulus parameterization has been modified with increased entrainment and rain evaporation and changes in the convective downdraft as detailed in Del Genio et al. (2012). For example, the stronger entrainment allows the new cumulus parameterization to produce Madden–Julian oscillation (MJO)-like variability (Kim et al. 2012). The boundary layer turbulence parameterization has been modified as well in the P5 simulation (Yao and Cheng 2012). According to Yao and Cheng (2012), this new scheme differs in its computation of nonlocal

TABLE 1. Most commonly used or referred to acronyms in this text are listed alphabetically within this table.

Acronym	Full definition	Acronym	Definition
AIRS	Atmospheric Infrared Sounder	LW	Longwave
AMIP	Atmospheric Model Intercomparison Project	MBL	Marine boundary layer
ASMR-E	Advanced Microwave Scanning Radiometer for EOS	NASA	National Aeronautics and Space Administration
C5	Denotes GISS CMIP5 results	OLR	Outgoing longwave radiation
CE/CM	Denotes (CERES/CERES-MODIS) results	P5	Denotes GISS post-CMIP5 results
CERES	Clouds and the Earth's Radiant Energy System	PBL	Planetary boundary layer
CF	Cloud fraction	PWV	Precipitable water vapor
CMIP	Coupled Model Intercomparison Project	RH	Relative humidity
CRE	Cloud radiative effect	RMSE	Root-mean-square error
CWP	Cloud water path	SML	Southern midlatitude
DW	Downwelling	SST	Sea surface temperature
EBAF	Energy Balanced and Filled	SW	Shortwave
GCM	Global circulation model	TOA	Top of the atmosphere
IPCC	Intergovernmental Panel on Climate Change	UW	Upwelling

transports, turbulent length scale, and PBL height, and shows improvements in cloud and radiation simulations, particularly over the subtropical eastern oceans and the southern oceans, despite the fact that the stratiform cloud parameterization itself is unchanged from the C5 version. A detailed analysis of the C5 run can be found in Schmidt et al. (2014). The differences between the P5 and C5 model runs were discussed more extensively in Part I of our study, which had an identical setup of the GISS GCM.

b. *CERES EBAF-TOA*

The CERES (Wielicki et al. 1996) Energy Balanced and Filled at the top of the atmosphere (EBAF-TOA) Ed2.7 dataset is used for radiative comparisons in this study. The CERES EBAF-TOA product is derived using the CERES 1° synoptic radiative fluxes and clouds (SYN1deg)-lite product, adjusted within the uncertainty to be consistent with the net planetary imbalance derived from ocean heating rates from Argo in situ ocean temperature measurements (Loeb et al. 2012b). CERES TOA radiative fluxes data have been validated across multiple studies (Loeb et al. 2006, 2007; Kato and Loeb 2005; Doelling et al. 2013). For more detailed information regarding the derivation of CERES results, please consult the following sources: Loeb et al. (2001, 2003, 2005, 2012a), Kopp and Lawrence (2005), and Minnis et al. (2011a,b). Based on documentation, CERES EBAF regional errors/uncertainties, meaning more specifically average error across any singular $1° \times 1°$ grid box, are as follows: TOA clear-sky OLR ($3.6\,\mathrm{W\,m^{-2}}$) and TOA clear-sky SW ($2.6\,\mathrm{W\,m^{-2}}$). TOA all-sky SW errors/uncertainties are $\sim 5\,\mathrm{W\,m^{-2}}$ during the period of March 2000–June 2002 and $\sim 4\,\mathrm{W\,m^{-2}}$ during the period of July 2002–December 2010. Monthly mean fluxes were determined by the CERES team through spatially averaging the instantaneous values on a ($1° \times 1°$) grid, temporally interpolating between observed values at 1-h increments for each hour of every month, and then averaging all hour boxes in a month (Young et al. 1998; Doelling et al. 2013). Level-3 processing is performed on a nested grid, which uses 1° equal-angle regions between 45°N and 45°S, maintaining area consistency at higher latitudes. The fluxes from the nested grid are then output to a complete 360×180 ($1° \times 1°$) grid using replication. In the CERES EBAF-TOA data product, clear-sky TOA fluxes are supplemented with fluxes derived from partly cloudy CERES footprints via narrow-to-broadband regression (Loeb et al. 2009).

c. *Methodology*

1) CALCULATIONS OF AVERAGES: GLOBAL AND ZONAL MEANS

Global averages are calculated using two different methods in this study, based on the global property being averaged. Specifically, global averages of albedo must be calculated in a manner that differs from other variables. For most variables, the data within each grid box are averaged into an array of 12 months (from January to December) by averaging like months, such as every March from 2000 to 2005. This helps to account for the missing months associated with beginning this study in March of 2000. After this, the values of each grid box for all 12 months are averaged to generate a yearly mean for the aforementioned grid box, generating a global grid of yearly means, as is shown in all global plots. Zonal averages (as seen in Figs. 4 and 8) are generated from the gridded global means by averaging across latitudinal bands. In this method, a cosine-weighting scheme is employed to calculate the total global average, where each point is weighted by the cosine of the latitude. A global average is finally calculated by the ratio of the sum of the values to the sum of the weights. As mentioned prior, our method for calculating the global mean albedo differs

slightly from this procedure. Given that albedo is a ratio of reflected SW to downwelling SW, our previous method leads to erroneous global averages. Instead, global averages of albedo are calculated using the ratio of the sum of the weighted reflected SW to the sum of the weighted downwelling SW. That is, values of reflected SW and downwelling SW are weighted using the cosine-weighting scheme mentioned prior, summed up respectively across the globe, divided by the sum of the weights, and then the global mean albedo is calculated as the weighted sum of reflected SW over the weighted sum of downwelling SW.

2) CALCULATIONS OF CLOUD RADIATIVE EFFECT

CRE calculations in this study are derived using the standard methods found in previous studies (Ramanathan et al. 1989; Dong and Mace, 2003; Dong et al. 2006, 2010). As in previous studies, SW and LW CREs at TOA are calculated as the difference between the net TOA fluxes, downwelling minus upwelling, of measurements during all-sky conditions minus clear-sky conditions [as shown in Eqs. (1) and (2)]. Net CRE is calculated by summing both SW and LW CREs. Positive values of CRE indicate a radiative energy gain due to the presence of clouds, a warming effect, while negative values denote a radiative energy loss due to the presence of clouds, a cooling effect

$$\begin{aligned}\mathrm{CRE_{SW}(TOA)} &= (\mathrm{SW}^{\downarrow} - \mathrm{SW}^{\uparrow}_{\mathrm{all}}) - (\mathrm{SW}^{\downarrow} - \mathrm{SW}^{\uparrow}_{\mathrm{clear}}) \\ &= \mathrm{SW}^{\uparrow}_{\mathrm{clear}} - \mathrm{SW}^{\uparrow}_{\mathrm{all}} = \mathrm{SW}^{\downarrow}(R_{\mathrm{clear}} - R_{\mathrm{all}})\end{aligned} \tag{1}$$

and

$$\begin{aligned}\mathrm{CRE_{LW}(TOA)} &= (\mathrm{LW}^{\downarrow}_{\mathrm{all}} - \mathrm{LW}^{\uparrow}_{\mathrm{all}}) - (\mathrm{LW}^{\downarrow}_{\mathrm{clear}} - \mathrm{LW}^{\uparrow}_{\mathrm{clear}}) \\ &= \mathrm{LW}^{\uparrow}_{\mathrm{clear}} - \mathrm{LW}^{\uparrow}_{\mathrm{all}},\end{aligned} \tag{2}$$

where $\mathrm{SW}^{\uparrow}_{\mathrm{clear}}$ and $\mathrm{SW}^{\uparrow}_{\mathrm{all}}$ represent clear-sky and all-sky reflected shortwave radiation at TOA, R_{clear} and R_{all} represent clear-sky and all-sky albedos at TOA, and $\mathrm{LW}^{\uparrow}_{\mathrm{clear}}$ and $\mathrm{LW}^{\uparrow}_{\mathrm{all}}$ represent clear-sky and all-sky OLRs, respectively.

3. Analysis of global results

Note that the errors in satellite retrieved results are not explicitly accounted for in the figures shown in this study. While satellite retrievals do contain uncertainties and biases, they remain good tools for diagnosing model issues. The readers should note that given this caveat about satellite retrievals and uncertainty, the term "bias" used in this paper is in its simplest form, and represents the difference between the model simulations and the observations. In this section, we compare the global patterns of clear-sky and all-sky outgoing longwave radiation, albedo, and cloud radiative effects, simulated by the GISS GCMs (P5 and C5) at TOA, with the CERES-retrieved cloud and radiation results. Many of these variables were compared by Dolinar et al. (2014) across 28 GCMs participating in CMIP5. Dolinar et al. (2014) found that while the differences in reflected shortwave flux and OLR between the ensemble mean (28 GCMs) and observations are small, there is a wide spread in results from the individual models. LW, SW, and net CREs are also shown to have a large spread between the models, particularly over the midlatitude and tropical regions. The multimodel ensemble mean cloud fraction (57.6%) and cloud water path are, on average, underestimated by nearly 8% and 16.1 g m^{-2} when compared to CERES-MODIS results. Based on the results of Part I of this study, as well as the biases found in Dolinar et al. (2014), we compare global and regional biases in detail using the newly modified (cumulus and boundary layer turbulence parameterizations) P5 simulation and compare it with its predecessor C5 against CERES observations.

a. Outgoing longwave radiation

Figures 1a–c show observed and modeled gridded annual clear-sky OLRs for CE, P5, and C5, respectively; Figs. 1d and 1e show the differences between simulated and observed clear-sky OLRs, P5 − CE and C5 − CE, respectively. Statistics of means, standard deviations, biases, RMSE, and spatial correlations for all variables, based on global results, are shown in Table 2. Zonal averages of clear-sky OLR for CE, P5, and C5 are shown later (in Fig. 5a). Overall global patterns of clear-sky OLR appear to be fairly well represented in both the P5 and C5 simulations. It is shown, however, in Figs. 1d and 1e that both the P5 and C5 simulations appear to underestimate the CE observed clear-sky OLR globally by ~4 and ~8 W m^{-2}, respectively. This discrepancy is in part due to the known clear-sky OLR dry bias when comparing GCM simulations to observations.

The dry bias occurs as a result of the differing methods used between the GCMs and observations to interpret OLR for clear-sky scenes. To derive the clear-sky OLR, the CERES science team identifies the cloudiness of scenes from CERES-MODIS observations using CERES cloud mask algorithms. This results in clear-sky OLR retrievals under truly clear-sky conditions. GCMs, however, are capable of removing the cloud contamination within a scene to calculate clear-sky OLR for clear conditions. As discussed in Sohn et al. (2006), while the clouds are technically removed, the dynamic and thermodynamic conditions that made it favorable to

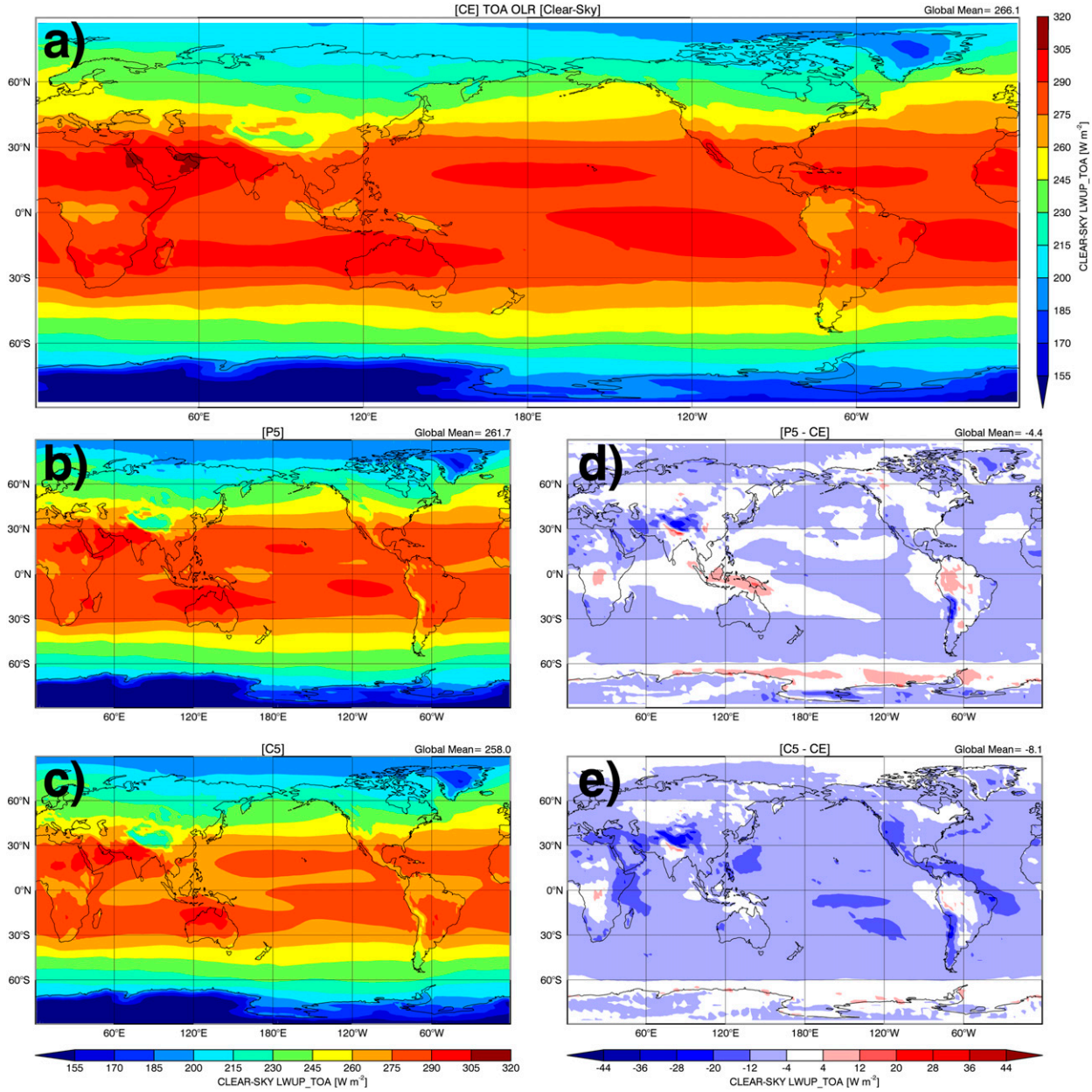

FIG. 1. Gridded annual mean clear-sky outgoing longwave radiation (OLR) at top-of-atmosphere (TOA) derived from (a) NASA CERES EBAF (CE) results, and simulated by NASA GISS (b) post-CMIP5 (P5) and (c) CMIP5 (C5) simulations, as well as their differences (d) P5 − CE and (e) C5 − CE, for the period from March 2000 through December 2005.

form clouds are still present. More specifically, the modeled hypothetical clear-sky humidity in cloudy regions is wetter than the cloud-free regions identified by the CERES cloud mask. Sohn and Bennartz (2008) found that the redistribution of water vapor associated with convection results in a significant contribution to LW CRE through the upper tropospheric moistening in the tropics, whereas columnar water vapor variation dominates OLR over the midlatitudes. Therefore, the CERES observed clear-sky OLR for a scene may be higher than modeled clear-sky OLR, simply on the basis that it is calculated from selected cloud-free pixels, which likely represents drier atmospheric conditions for a given location.

Kato et al. (2013) examined the impact of the dry bias globally, and found a mean difference of $-1.25\,\mathrm{W\,m^{-2}}$ between a cloud-removed modeled atmosphere and observed clear-sky data. Based on this result, the dry bias can only explain a portion of the clear-sky OLR bias

TABLE 2. Statistics of global means, standard deviations, biases in the global means, RMSE, and pattern correlations were calculated using annual-mean maps to compare both models with CERES observations. The last column serves as a quick lookup table that displays if the standard deviation, global mean bias, RMSE, and correlation in the P5 simulation improved (I), worsened (W), or remained constant (-), respectively, when compared to its C5 predecessor.

Variable	Dataset	Mean	Std dev	Bias	RMSE	Correlation	Quicklook
OLR (CLR-SKY) ($W\,m^{-2}$)	P5	261.7	42.1	−4.4	5.94	0.99	W, I, I, -
	C5	258.0	39.9	−8.1	8.19	0.99	
	CE	266.1	40.8	—	—	—	
OLR (ALL-SKY) ($W\,m^{-2}$)	P5	240.9	35.9	+1.1	6.90	0.98	I, W, W, -
	C5	239.6	34.6	−0.2	6.84	0.98	
	CE	239.8	35.7	—	—	—	
Albedo (CLR-SKY) (%)	P5	0.153	0.206	−0.001	0.051	0.98	W, I, W, -
	C5	0.157	0.195	+0.003	0.041	0.98	
	CE	0.154	0.188	—	—	—	
Albedo (ALL-SKY) (%)	P5	0.295	0.164	+0.002	0.036	0.98	I, W, I, I
	C5	0.294	0.149	+0.001	0.041	0.97	
	CE	0.293	0.160	—	—	—	
SW absorption (CLR-SKY) ($W\,m^{-2}$)	P5	289.4	112.0	+1.5	8.36	0.99	W, W, W, -
	C5	287.9	108.4	+0.2	7.85	0.99	
	CE	287.7	107.0	—	—	—	
SW absorption (ALL-SKY) ($W\,m^{-2}$)	P5	241.0	96.1	+0.3	9.33	0.99	I, I, I, -
	C5	241.2	90.3	+0.6	15.02	0.99	
	CE	240.6	95.2	—	—	—	
LW CRE ($W\,m^{-2}$)	P5	20.8	10.9	−5.5	7.80	0.89	I, I, I, -
	C5	18.3	9.3	−8.0	9.46	0.89	
	CE	26.3	11.8	—	—	—	
SW CRE ($W\,m^{-2}$)	P5	−48.4	25.5	−1.2	9.38	0.93	W, W, I, I
	C5	−46.8	22.9	+0.4	14.80	0.80	
	CE	−47.2	23.5	—	—	—	
Net CRE ($W\,m^{-2}$)	P5	−27.7	18.2	−6.8	10.54	0.86	W, I, I, I
	C5	−28.5	15.7	−7.6	13.86	0.66	
	CE	−20.9	15.7	—	—	—	

found in this study. Comparisons of clear-sky OLR (in Fig. 5a) show that observed clear-sky OLRs are slightly higher than both the P5 and C5 results over the midlatitudes and tropical regions. Sohn and Bennartz (2008) compared the AMSR-E derived all-sky PWVs with those having a liquid water path less than 5 and 30 $g\,m^{-2}$ and found that on average the difference between all-sky and clear-sky PWV is approximately 2 mm or 2 $g\,m^{-2}$. This result was consistent with our findings in Part I (see Fig. 6 therein), where the AIRS PWV, which is known to be dry biased due to the lack of retrievals in overcast conditions, is ~2 mm lower than both AMSR-E and P5 PWV when compared over the oceans. It should also be noted that P5 employs a new cumulus parameterization scheme. This scheme modifies convection within the model, making convection generally shallower with less water vapor being detrained into the upper troposphere and more in midtroposphere. This effect would increase OLR within the P5 simulation, as is observed in Fig. 1. It is hypothesized that PWV cannot solely explain the differences observed in clear-sky OLR, warranting further study to explore these biases in clear-sky OLR.

For all-sky OLR comparisons, while the P5- and C5-simulated global distributions of OLR are fairly similar to CERES observations and their global means are within ~1 $W\,m^{-2}$ (Fig. 2), large differences exist regionally between the models and the observation. These regional differences can be partially explained by our all-sky PWV comparisons from Part I (see Fig. 5 therein). For example, the large negative biases (see P5 − CE and C5 − CE in Figs. 2d,e) of all-sky OLR around the central Pacific (~0°, 180°) and positive biases over Indonesia and Australia have strong negative correlations with their corresponding PWV comparisons from Part I (see Figs. 5e,f therein). Regional biases of all-sky OLR also agree well with the total column CF comparisons presented in Fig. 1 of Part I. More specifically, regions with a strong positive bias in total column CF correspond well with lower all-sky OLR due to the lower LW emission of colder cloud-top temperatures. On the other hand, regions with a strong negative bias in total column CF correspond well with higher values of all-sky OLR due to the higher emission associated with warmer surface temperatures. No significant differences in all-sky OLR are found over the SMLs, where P5-simulated low-level

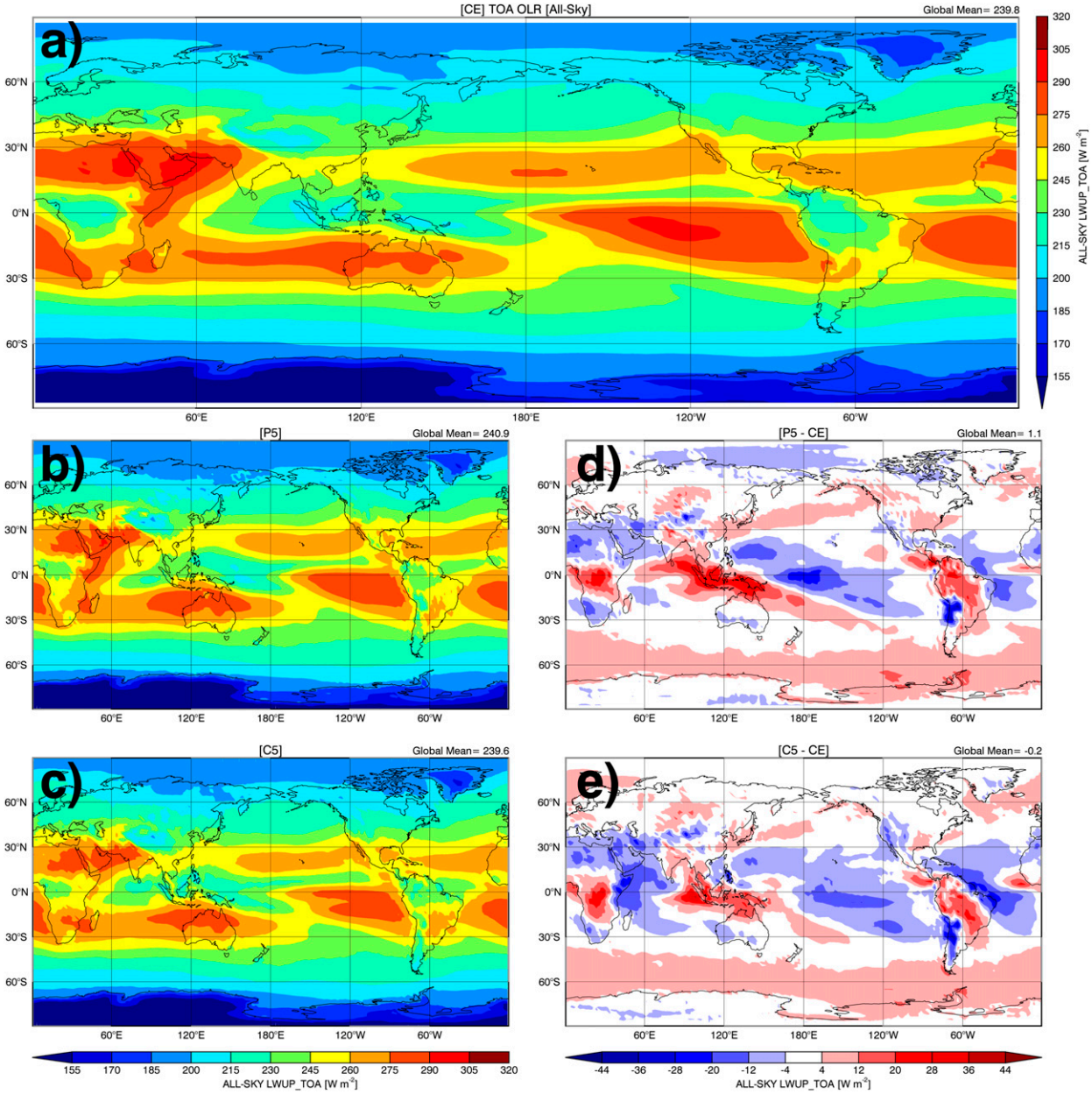

FIG. 2. As in Fig. 1, but for all-sky OLR at TOA.

CF has increased by ~20%, as discussed in Part I. It is expected that these clouds have only a small impact on all-sky OLR due to the small variation between cloud-top temperature of low-level clouds and the sea surface temperatures below.

Comparing zonally averaged OLR in Fig. 5b, the P5-simulated all-sky OLRs agree well with the CE observation, which is consistent with the good agreement found between P5 and AMSR-E zonally averaged PWV in Part I (Fig. 6b therein). However, examining biases in all-sky OLR on a regional scale shows that this result is due to offsetting biases within the GCMs. Large regional biases are examined further in section 4 of this study under differing dynamical regimes. The all-sky OLR comparisons have led us think about investigating the impact of total CF and PWV on all-sky OLR over some regions in this study.

b. Albedo

Clear-sky TOA albedos are shown in Figs. 3a–c for CE observations and P5 and C5 simulations, respectively, with their corresponding differences, P5 − CE and C5 − CE,

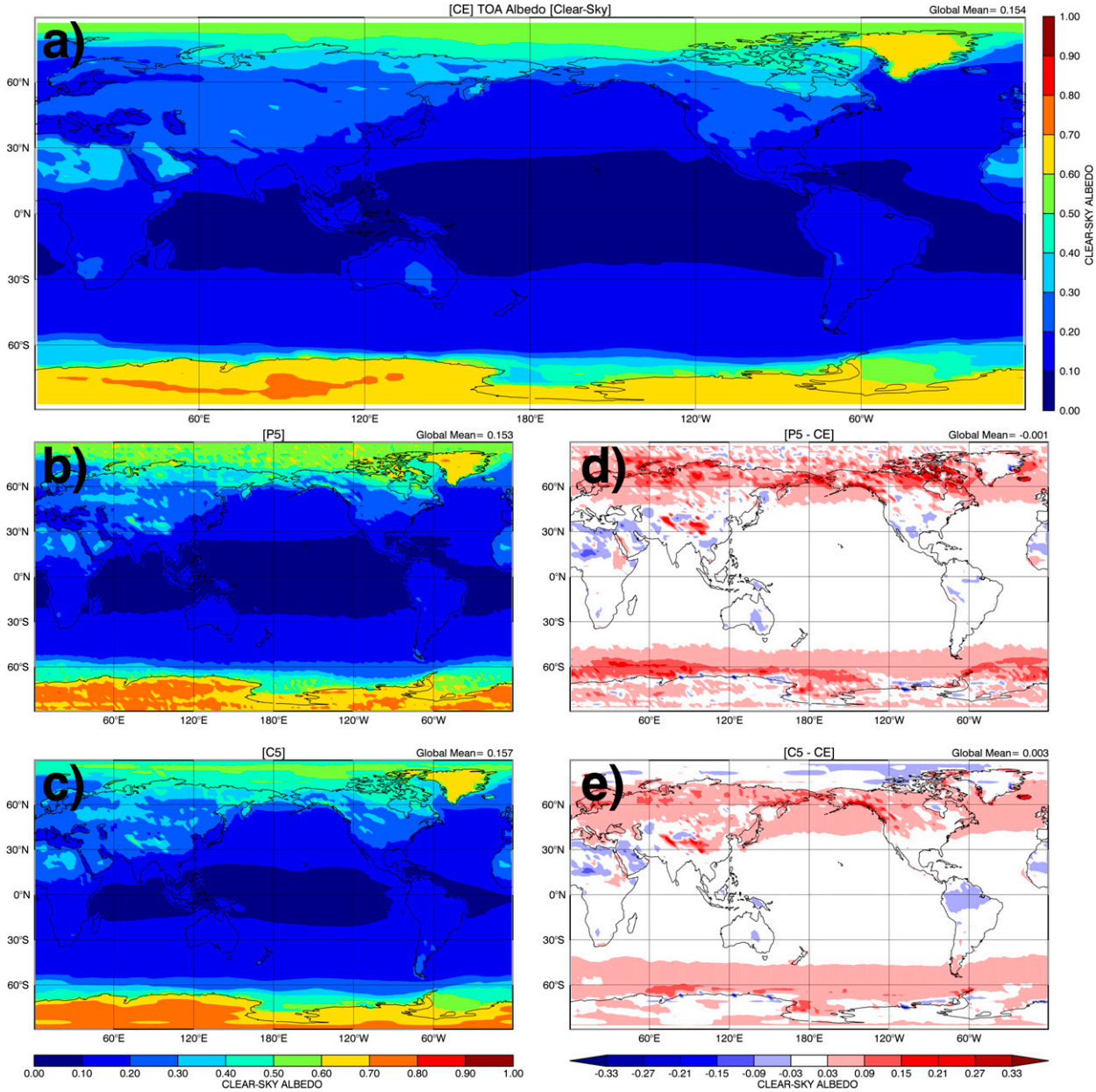

FIG. 3. As in Fig. 1, but for clear-sky TOA albedo.

shown in Figs. 3d and 3e. All-sky TOA albedos are plotted in the same manner as clear-sky results in Fig. 4. Zonal averages of clear-sky and all-sky albedos are presented in Figs. 5e and 5f, respectively.

As illustrated in Figs. 3 and 5, the modeled global mean clear-sky albedos agree with CE observation to within 0.01. When comparing the regional differences in clear-sky albedo between the models and CE observations (Figs. 3d,e), all results agree well with each other within ±50° latitude. Outside of ±50° latitudes, both P5 and C5 have positive biases that can be seen both regionally (Figs. 3d,e) and zonally (Fig. 5e). These biases are potentially due to the differences in clear-sky surface albedo between the observations and those used in the GISS models. This is particularly true closer to the poles where clear-sky albedo is heavily influenced by sea ice albedo, which can be affected by the age of the ice, the presence of snow on the ice, or the formation of melt ponds. While zonal patterns of clear-sky albedo (Fig. 5e) show disagreement outside ±50° latitude, zonal patterns of clear-sky SW absorption show agreement across nearly all latitudes, as shown in Fig. 5c.

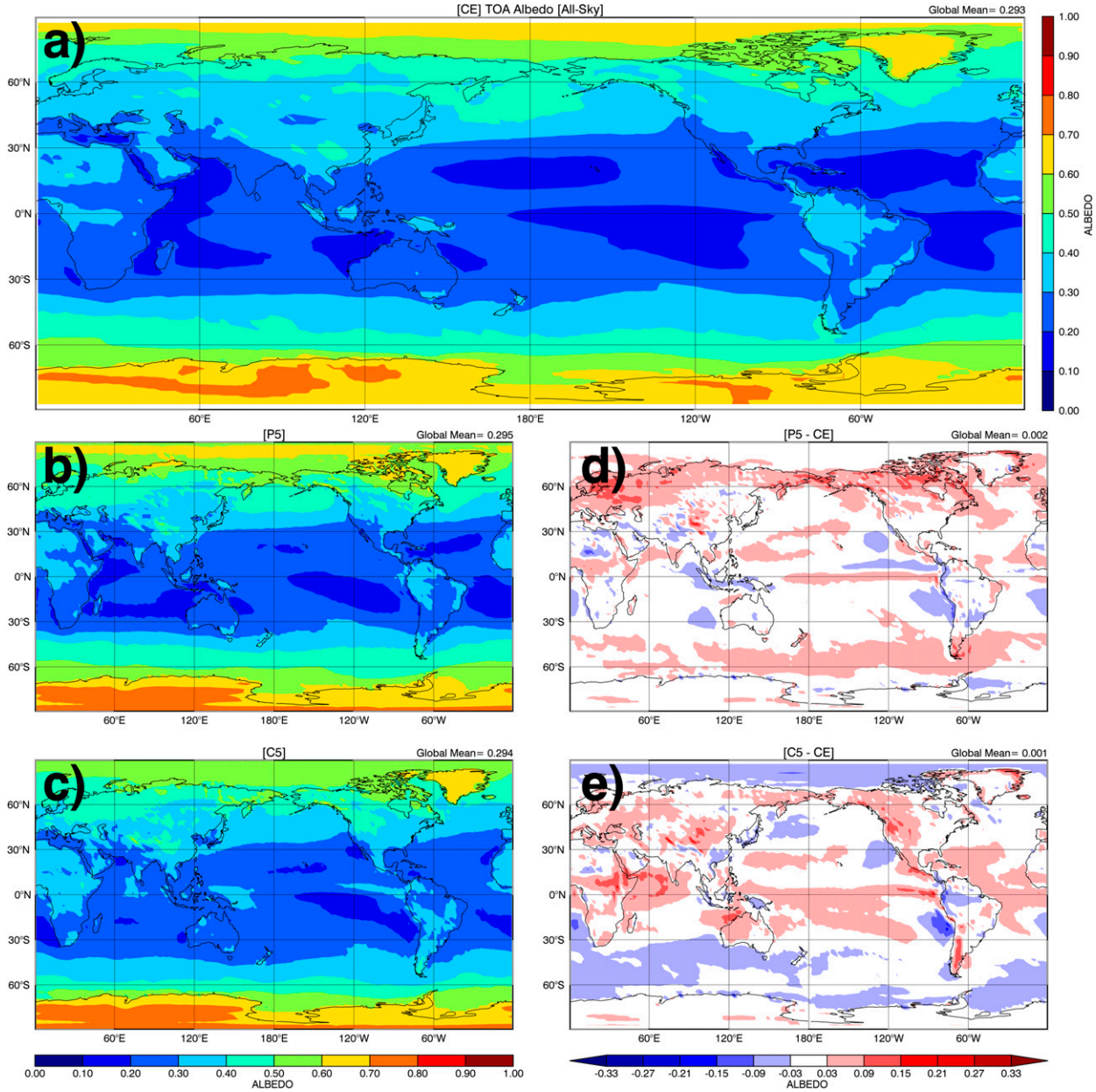

FIG. 4. As in Fig. 1, but for all-sky TOA albedo.

While a quick comparison of global mean all-sky albedos suggests a good agreement between the models and observations, large biases are found regionally between the models and CE observations (Figs. 4d,e). The regional bias patterns in both the P5 and C5 simulations are similar to those in their total column CF comparisons (Figs. 1e and 1f; see Stanfield et al. 2014). For example, the P5-simulated total column CF over the SMLs has increased ~20% compared to the previous C5 simulation (Figs. 1 and 2 of Part I). This increase in CF has resulted in increased all-sky albedos (Figs. 4f and 5f) and decreased SW absorption at TOA (Fig. 5d) in the P5 simulation over the SMLs. P5-simulated all-sky albedos have improved in regions with a known high frequency of MBL clouds, such as off the western coast of North and South America, due to the increase in CF from the newly implemented PBL scheme. We will discuss these regional details further in section 4.

c. *Cloud radiative effects*

LW CREs are shown in Fig. 6, with CE, P5, and C5 LW CREs shown in Figs. 6a–c, respectively, while their

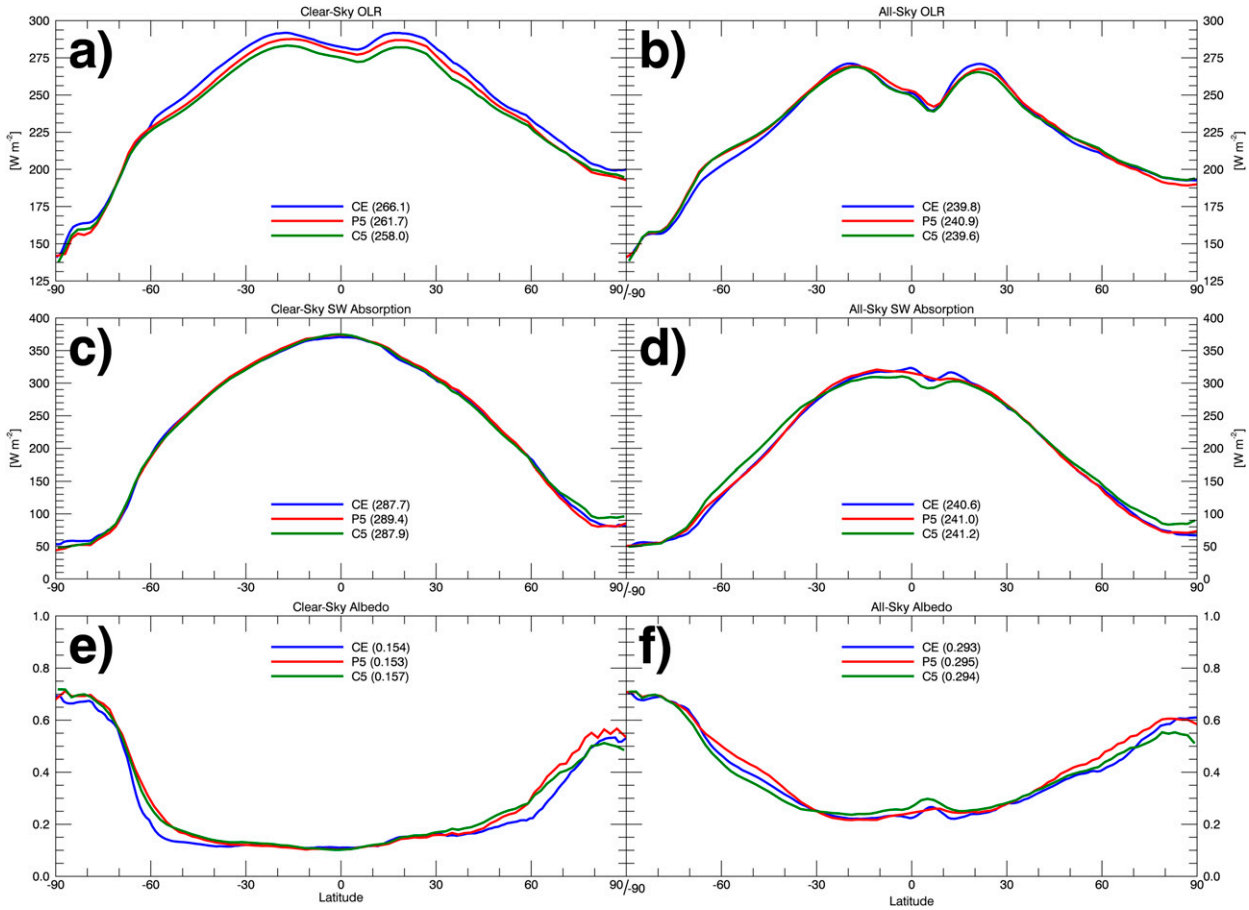

FIG. 5. Zonally averaged clear-sky and all-sky (a),(b) OLR, (c),(d) SW absorption, and (e),(f) albedo for CE (blue), P5 (red), and C5 (green).

corresponding differences, P5 − CE and C5 − CE, are shown in Figs. 6d and 6e, respectively. The overall global patterns of simulated LW CREs from both P5 and C5 agree fairly well with CE observations. Clouds have a warming effect on the TOA LW radiation budget with a global average of 26.3 W m^{-2} based on CE observations, while P5 and C5 averages are −5.5 and −7.9 W m^{-2} lower than the observation, respectively. Global means of LW CRE and all-sky and clear-sky OLRs suggest that clear-sky OLR is the main contributor of biases in LW CRE; however, regional analysis suggests a more complicated relationship. Taking into account the potential dry bias, comparing PWV in Fig. 5 from Part I of this study with LW CRE in Fig. 6 of this study suggests a strong correlation between PWV results and LW CRE. However, the cloud contribution to LW CRE cannot be ignored. For example, the LW CREs (Figs. 6a–c), excluding the polar regions, have strong correlations with CFs shown in Part I of this study (Figs. 1a,c,d). The LW CRE differences shown in Figs. 6d and 6e also mimic the patterns of their corresponding CF differences (P5 − CM and C5 − CM in Figs. 1e,f of Part I, where CM denotes CERES-MODIS). Therefore, it can be concluded that clouds and PWV both play major roles in calculating LW CRE (Sohn et al. 2006; Sohn and Bennartz 2008; Dong et al. 2006).

For SW CRE, PWV does not play as important of a role as clouds (Dong et al. 2006). In contrast to the warming effect on the TOA LW radiation budget, clouds have a strong cooling effect on the TOA SW radiation budget, particularly low-level clouds, with a global average of −47.2 W m^{-2} based on CE observations. Although both the P5 and C5 global averages agree with the observation within ~1 W m^{-2}, large differences occur regionally. The global distributions of P5 − CE and C5 − CE SW CRE (Figs. 7d,e) have demonstrated that the C5-simulated SW CREs tend to have larger regional differences than the P5 simulation when compared to the CE observation. For instance, as discussed previously and in Part I, the MBL CFs simulated by P5 have increased by ~20% compared to the C5 simulations over the SMLs. This increase brings the P5-simulated MBL clouds over

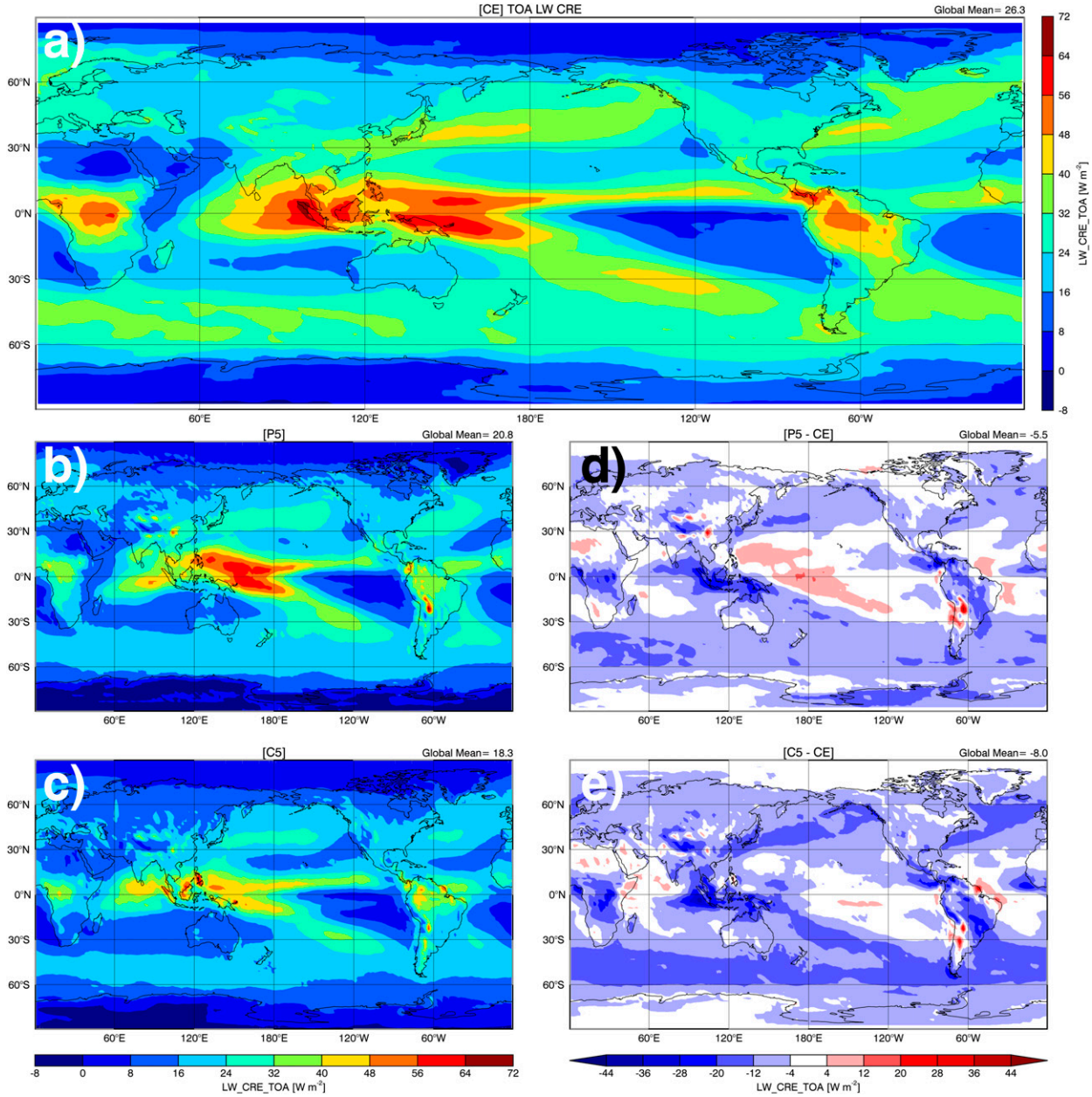

FIG. 6. As in Fig. 1, but for LW cloud radiative effect (CRE).

the SMLs much closer to CM observations (Fig. 1e in Part I), which results in a much better agreement in SW CRE between the P5 simulation and CE observations over the SMLs (Fig. 7d). On the opposite side, large positive biases exist in C5 simulations (Fig. 7e) due to large negative biases in C5-simulated MBL clouds over the SMLs (Fig. 1f in Part I). The SW and LW CREs over the polar regions should be used with caution given the highly reflective snow and ice surfaces common in these regions, where surface albedos are close to, if not higher than, cloud albedos (Dong et al. 2010).

Net CRE, shown in Fig. 8, is defined as the sum of LW and SW CREs and tends to be dominated by the SW cooling effect. The globally averaged net CREs are −20.9, −27.7, and $-28.5\,\mathrm{W\,m^{-2}}$ from CE, P5 and C5, respectively, indicating a net cooling effect of clouds on the TOA radiation budget. On a global mean basis, differences in global net CRE appear to be derived from biases in LW CRE. Examining LW, SW, and net CREs on a regional basis again suggests a more complicated relationship. For example, regions with a high frequency of marine boundary layer clouds are typically associated with

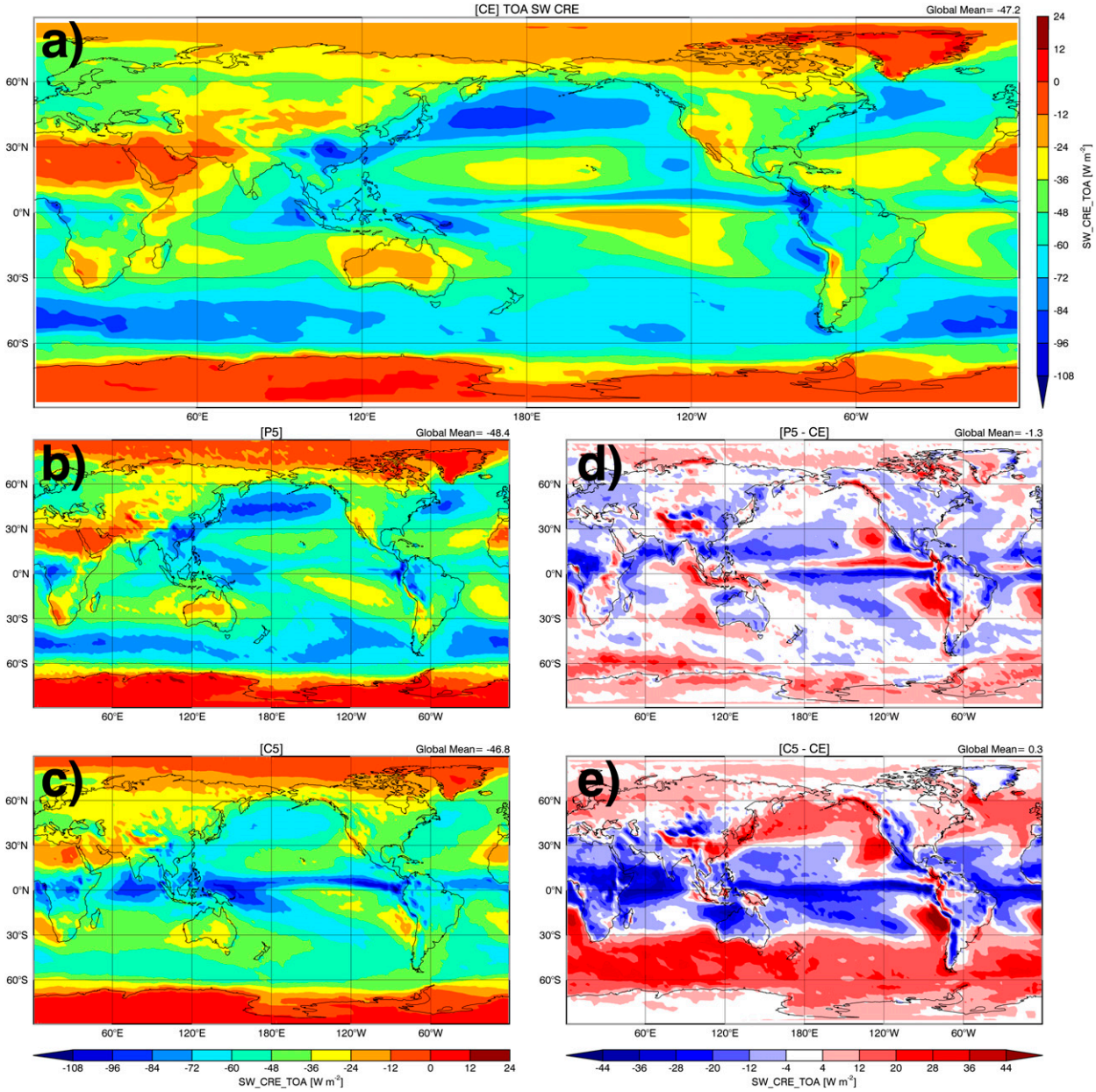

FIG. 7. As in Fig. 1, but for SW CRE.

large-scale atmospheric downwelling motion (Dong et al. 2014), such as off the western coast of the United States or South America. Here, both P5 and C5 tend to overestimate net CRE because the oversimulation of SW CRE outweighs the undersimulation of LW CRE. Over the SMLs, the P5-simulated SW CREs are closer to the CE observations due to the increase of MBL clouds within the P5 simulation; however, LW CRF is underestimated, which results in an undersimulation of net CRE over the SMLs.

To investigate the impact of cloud fraction and cloud water path on CREs, we plot the zonal means of LW, SW, and net CREs, as well as CF and CWP from Part I, in Fig. 9. The focus of this section will be shifted away from the SMLs, and will instead be focused more on the tropics. Over the tropics, the P5- and C5-simulated CFs agree well with CM observations, while their CWPs are much higher than CM. The clear-sky OLR is primarily determined by surface temperature, SST, and atmospheric PWV, while determinations of all-sky OLR are largely affected by cloud-top temperatures, particularly in overcast conditions or in the presence of opaque clouds. In the tropics, this is in part due to the high

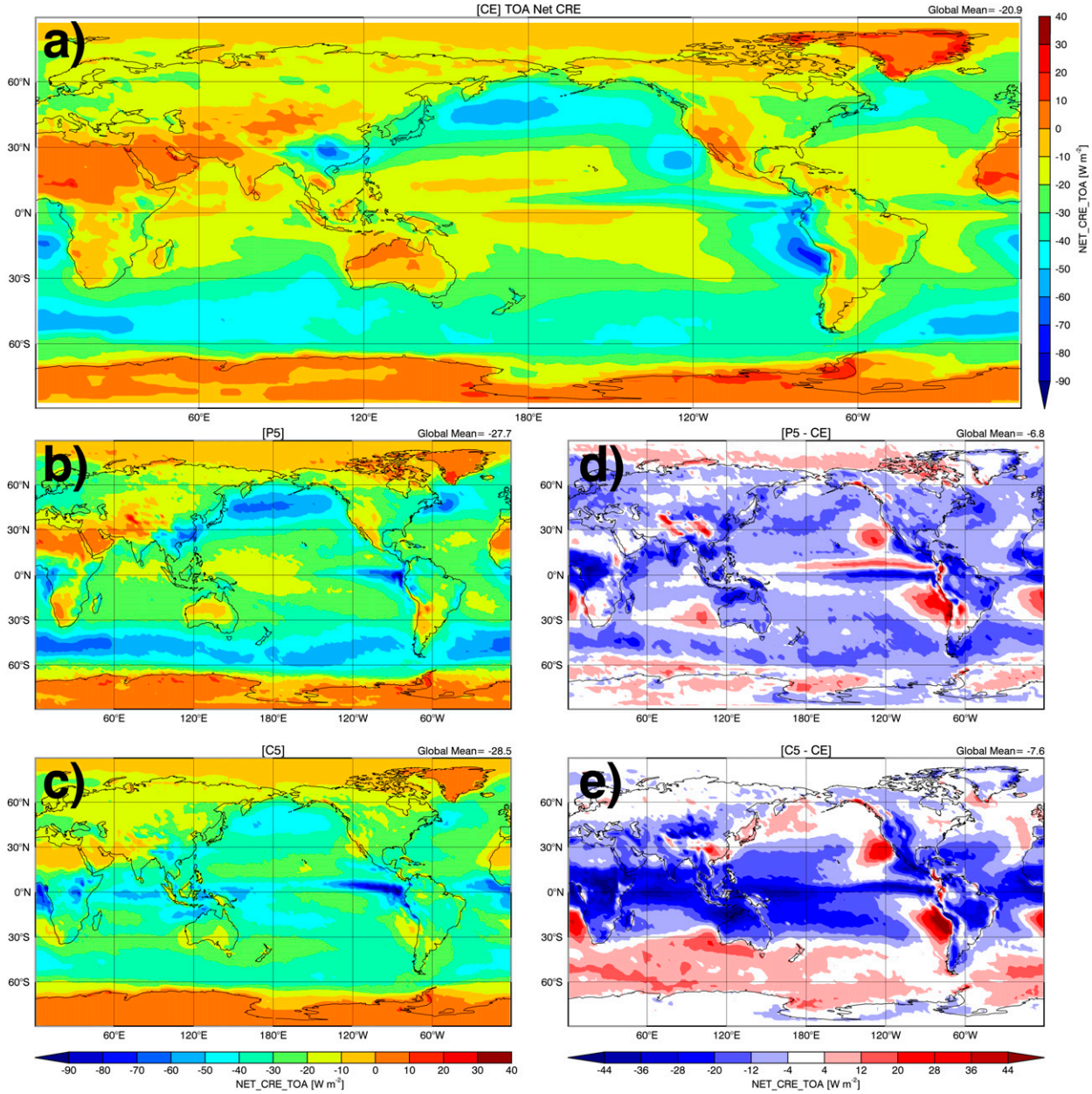

FIG. 8. As in Fig. 1, but for net CRE (SW CRE + LW CRE).

number of deep convective clouds that have cold cloud-top temperatures (~220 K; Dong et al. 2008). Therefore the LW CREs ($OLR_{clear} - OLR_{all}$) associated with these clouds should be fairly large and predominately determined by CFs, not CWP, given that most deep convective clouds are optically thick clouds (Dong et al. 2008). Given the good agreement in CF comparison and ignoring the differences in clear-sky OLR between P5–C5 and CM–CE, the LW CREs from these three datasets should be close to each other over the tropics. The much higher CWPs found in P5 and C5 simulations, however, do have an impact on their TOA SW albedos, resulting in a much stronger cooling effect on the TOA SW radiation budget, with more obvious effects in the C5 simulation. Net CRE zonal variations (Fig. 9e) essentially follow the variations of their corresponding SW CREs with slight modifications based on their corresponding LW CREs.

d. *Spatial and variability analysis using Taylor diagrams*

A Taylor diagram (Taylor 2001) is shown in Fig. 10 that illustrates the comparison between the P5–C5

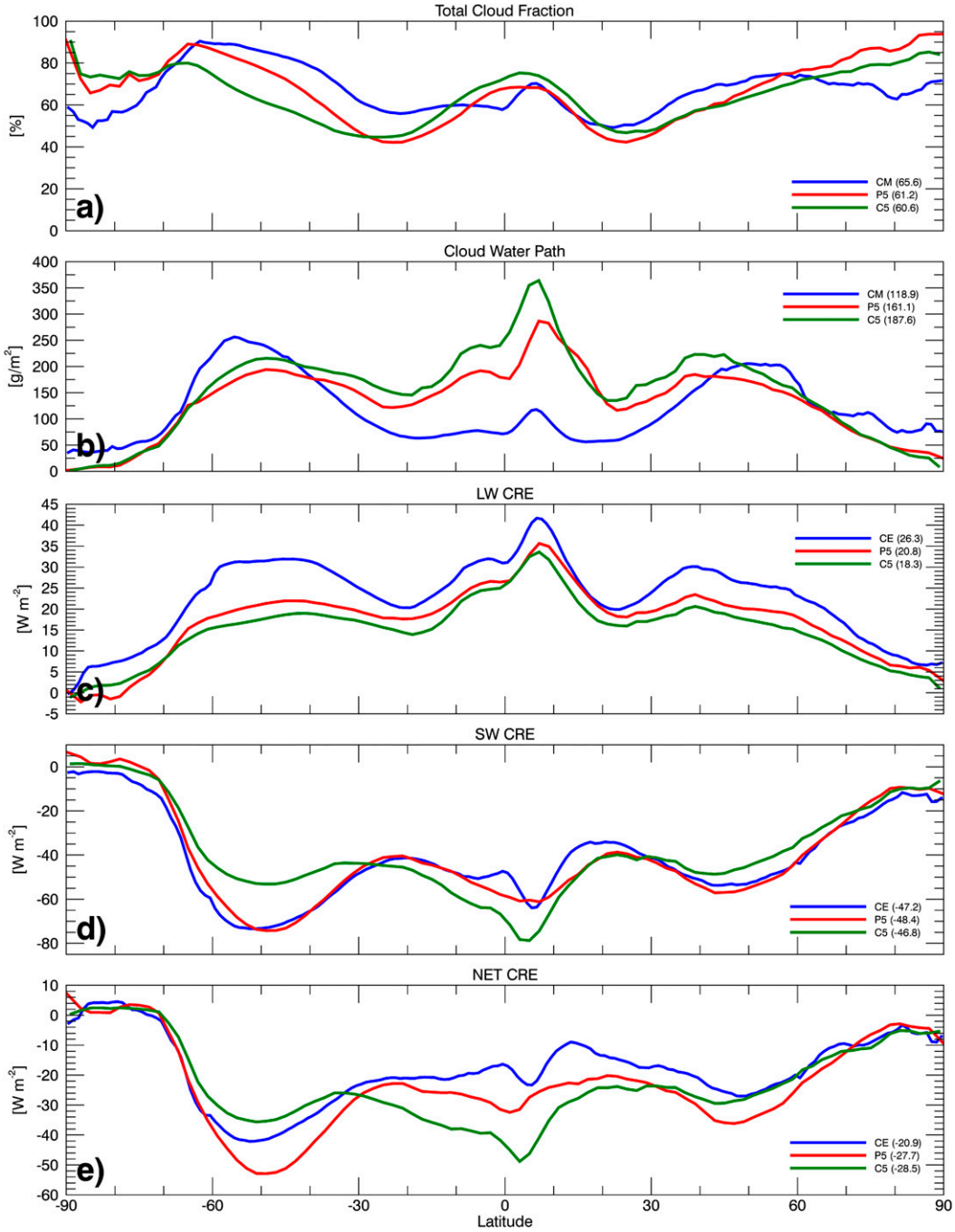

FIG. 9. Zonally averaged (a) cloud fraction, (b) cloud water path, (c) LW, (d) SW, and (e) net CREs for CE (blue), P5 (red), and C5 (green).

simulations and CE observations using standard deviations and correlations. Taylor diagrams summarize the differences in mean geographic patterns between model simulations and observations. Radii in Fig. 10 are given as normalized standard deviations, meaning specifically that the radii are calculated as the ratios of the standard deviation of the P5–C5 simulations to the standard deviation of the CE observation for a given variable. P5 (C5) results are shown in red (green) and prefaced with a letter P (C). The labels used in the diagram are outlined within the figure caption. If the model simulations agree well with observations, then

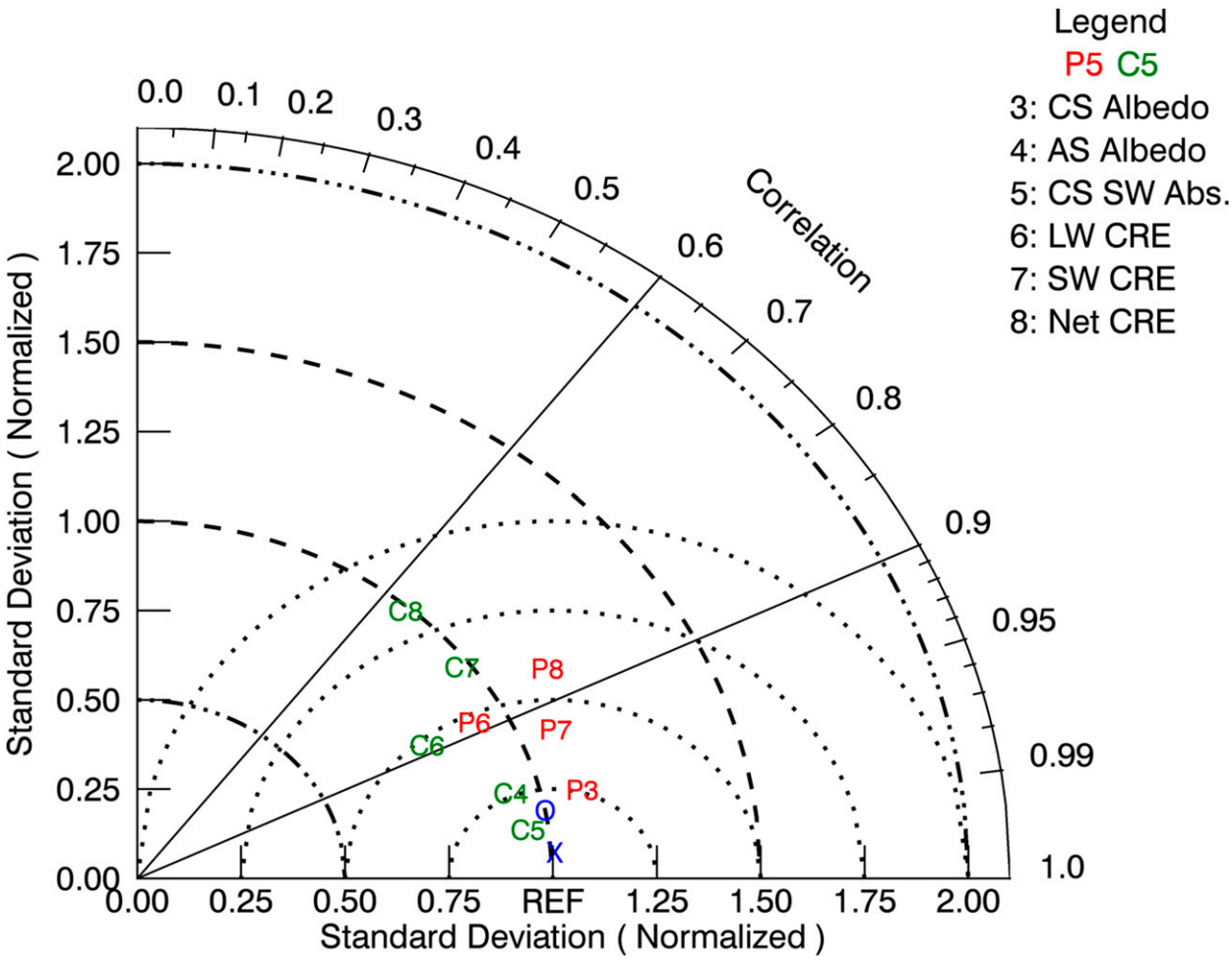

FIG. 10. Taylor diagram comparing P5 and C5 variables with CE observations. The provided legend defines labels used within the diagram, and is outlined as follows: P5 is in red with a preceding letter P, while C5 is in green with a preceding C. Label numbers used correspond with the figure number in which the variable is discussed. Not all variables are shown as many variables would overlap in this diagram. As such the blue X represents the position for the variables: P5 (LW CRE, SW CRE, and SW absorption) and C5 (LW CRE and SW CRE). The blue O represents the position for P5 (OLR and all-sky albedo) and C5 (OLR and clear-sky albedo). Correlations are located in the 7th column of Table 2. Normalized standard deviation can also be calculated using the deviations presented in the 4th column of Table 2. Concentric circles originating from the reference point (REF) represent lines of equal RMSE.

the simulated results will be located close to the reference point (REF) at one standard deviation and with a correlation of ~1 on the diagram. Compared to the cloud property comparisons presented in Part I, the P5–C5-simulated TOA radiation budget and net CREs agree much better with CE observations. Excluding CREs, all P5 and C5 simulations agree with observations within a normalized standard deviation of 0.75 to 1.25, and have correlations greater than 0.97. Note that a noticeable increase is shown in the correlations of SW and net CREs from the C5 to the P5 simulation. The correlation in LW CRE remains constant; however, an improvement in the variability of LW CRE is found in the P5 simulation compared to CE observations.

4. Regional analysis over downwelling and upwelling regimes and the SMLs

It has been shown in previous studies (e.g., Su et al. 2013) that model biases can be highly dependent on their dynamic regimes. For example, vertical pressure velocity (ω) at 500 hPa has been widely used as a proxy to examine model errors in regions of large-scale upwelling (UW; $\omega < 0$) and downwelling (DW; $\omega > 0$) motion (Bony and Dufresne 2005). To define these regimes, simulated fields of ω at or near 500 hPa, over the oceans, are shown in hectopascals per day for the P5 and C5 simulations in Figs. 11a and 11b, respectively. Although their global patterns are similar to each other, the P5 results tend to be slightly stronger and more

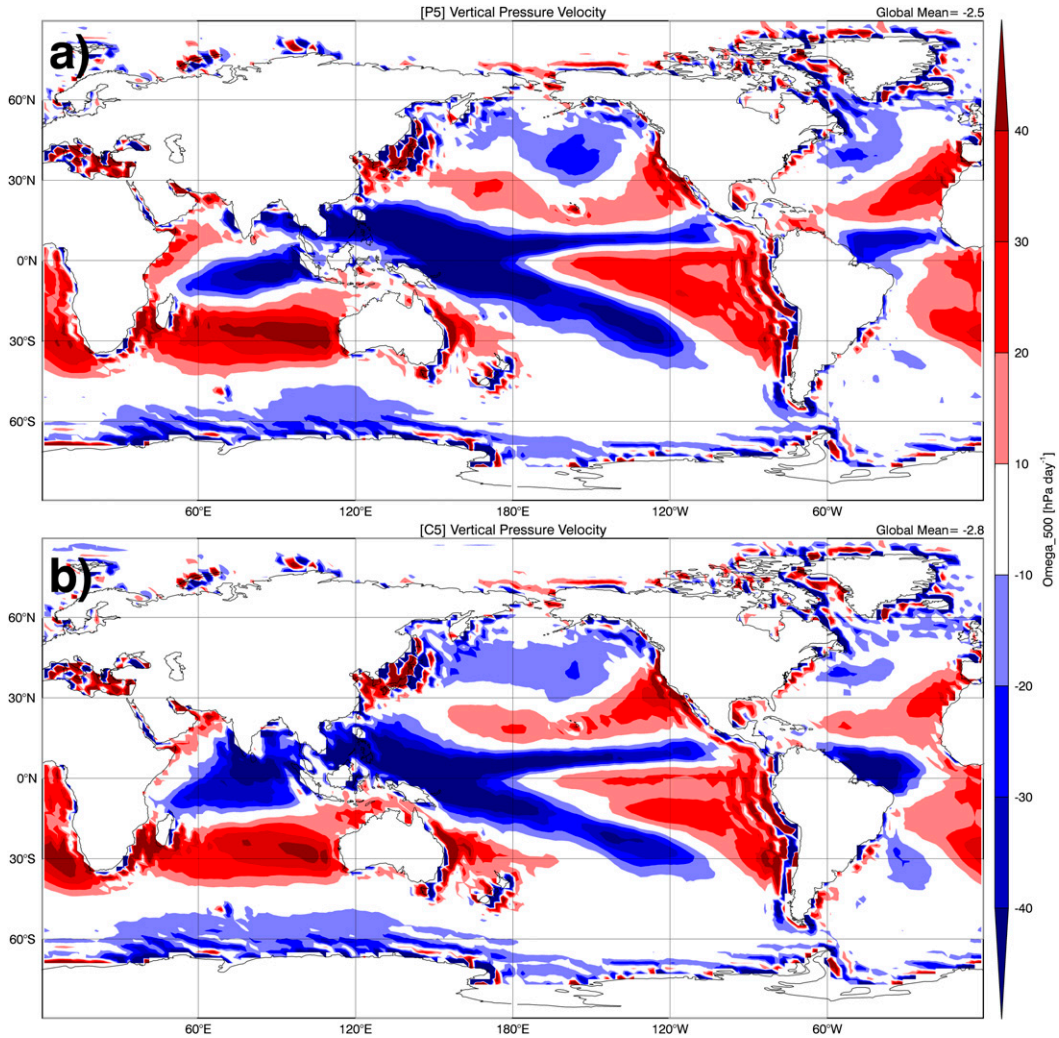

FIG. 11. Global maps of vertical pressure velocity (ω; hPa day^{-1}) near the 500-hPa level for the (a) P5 and (b) C5 simulations. Negative (positive) values indicate regions of upwelling (downwelling) motion. In this study, regions of strong atmospheric upwelling ($\omega < -25$ hPa day^{-1} at 500 hPa) and downwelling ($\omega > 25$ hPa day^{-1} at 500 hPa) have been selected to explore the regional differences between model simulations and observations.

widespread than the corresponding C5 results over both the UW and DW regimes. For this study, we analyze the cloud and radiative properties over regions of strong large-scale UW motion ($\omega < -25$ hPa day^{-1}) and DW motion ($\omega > 25$ hPa day^{-1}) within the tropics and subtropics ($\pm 40°$ latitude) (Dolinar et al. 2014).

Having defined both UW and DW regimes, we have compared the P5- and C5-simulated total column CFs, CWPs, and all-sky albedos over these two regimes with CERES-MODIS SYN1 and CERES EBAF observations (CM and CE). Compared to the CM observed CFs, the P5-simulated CFs outperform the previous C5 results in both UW (Fig. 12a) and DW (Fig. 12b) regimes, having higher spatial correlations and lower mean differences. Figures 12a and 12b show that both P5 and C5 oversimulate CF in regions of large-scale upwelling motion (Fig. 12a) while undersimulating CF in regions of downwelling motion. P5- and C5-simulated CWPs are shown to be biased roughly 2–4 times greater than CM observations within the defined UW regime, resulting in a low spatial correlations, large mean deviation, and large RMSEs. In comparison, the changes made to the new P5 parameterizations serve to further increase this bias. Within the DW regime, both P5- and C5-simulated results agree reasonably well with the CM observations, showing moderate correlations (0.67 and 0.53) and small RMSEs (~ 43 g m^{-2} and 55 g m^{-2}). The P5 simulation shows improved spatial correlation and decreased RMSE compared to its C5 counterpart in CWP over the DW regime. All-sky albedo comparisons across both

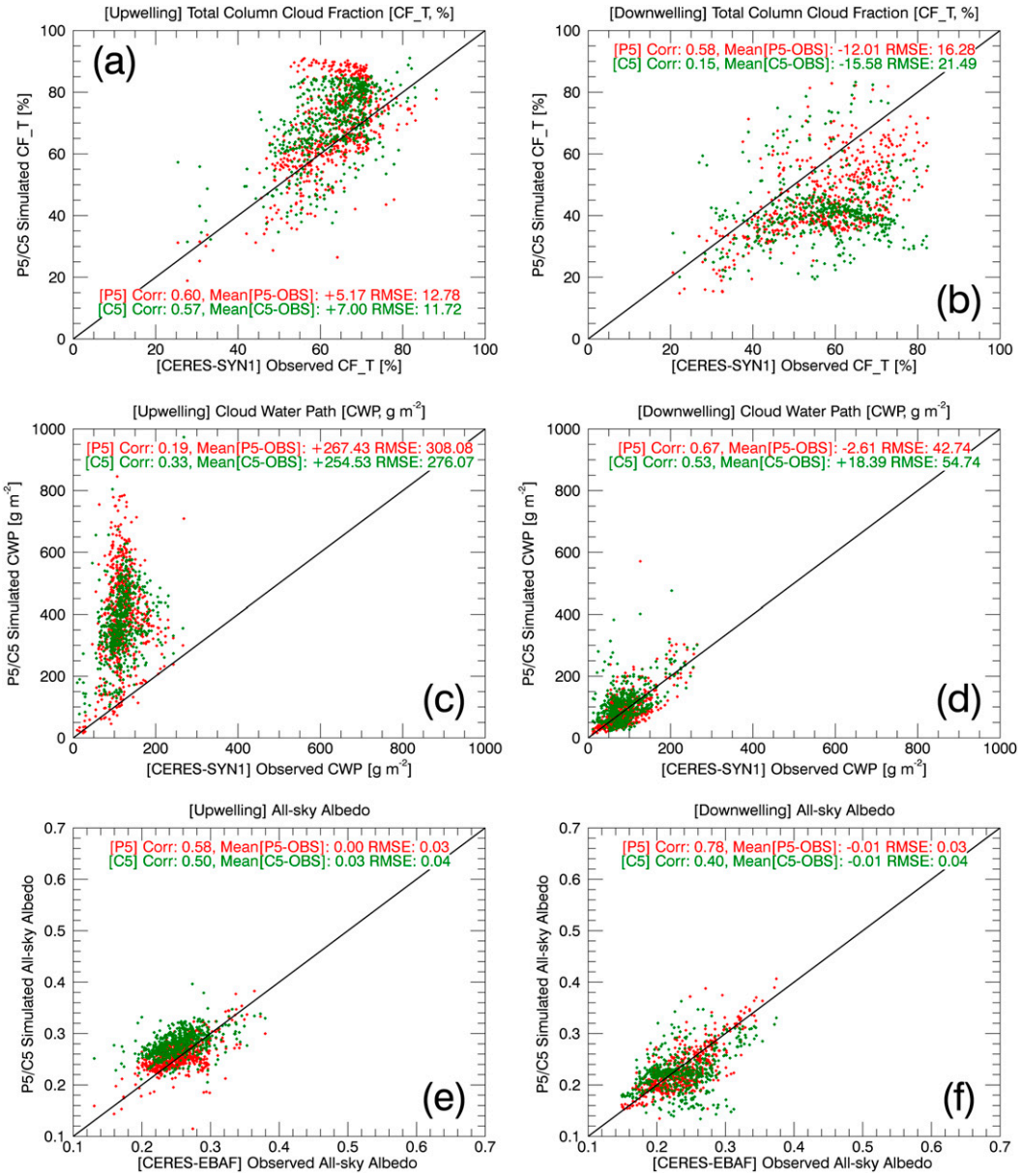

FIG. 12. Scatterplots of P5- and C5-simulated (a),(b) total column cloud fraction, (c),(d) cloud water path, and (e),(f) TOA all-sky albedo against CERES observations over defined regions of strong large-scale (left) upwelling and (right) downwelling vertical motion. The black line represents a perfect 1:1 correlation. Values of spatial correlation, mean difference between each model simulation and the observations, and RMSE are presented within each figure.

UW and DW regimes are similar to our previous CF comparisons. More specifically, the P5-simulated all-sky albedos show slight improvement within the UW regime (Fig. 12e) while showing significant improvement within the DW regime, where the correlation to CE observations increased from 0.40 to 0.78 (Fig. 12f).

In summation, although the all-sky albedos simulated by both P5 and C5 are close to the CE observations within the UW regime, both the P5 and C5 simulations moderately overestimate total column CF while drastically oversimulating CWP. Within the DW regime, both the P5- and C5-simulated all-sky albedos and CWPs agree well with the CERES observations; however, their simulated total column CFs are lower (~14%) than the observations. Although the differences in all-sky albedo between the P5–C5 simulations and CERES observations

in both regimes are fairly small, they are not well correlated with our CF and CWP comparisons. All-sky albedos depend primarily on both CF and CWP. As such, all-sky albedo comparisons are expected to be consistent with, or complementary to, CF and CWP comparisons, such as lower–higher CF and larger–smaller CWP, respectively. However, all-sky albedo comparisons within the UW regime do not make sense, physically, when the agreement found in all-sky albedo (Fig. 12e) is a result of similar biases in both CF (Fig. 12a) and CWP (Fig. 12c). Further study within the defined DW regime has revealed that while total column CF is ~14% lower than the CERES observations, the good agreements found in all-sky albedo and CWP comparisons can be explained from an increase in highly reflective low-level CF (pressure > 660 hPa, ~10%), and decreases in midlevel (660 hPa < pressure < 440 hPa, ~1%) and high-level CFs (pressure < 440 hPa, ~6%) (multilevel CFs not shown here).

High-level CF (pressure < 440 hPa), PWV, and all-sky OLR comparisons over the UW and DW regimes are shown in Fig. 13. Both the P5- and C5-simulated PWVs have an excellent agreement with the AMSR-E observations, with nearly perfect correlations over both regimes. An increase of $\sim 2\,\mathrm{g\,m^{-2}}$ is noted in the P5 simulation when compared to C5, which matches the $\sim 2\,\mathrm{g\,m^{-2}}$ increase in global mean PWV shown in Fig. 5 of Part I of this study. This increase in P5-simulated PWV is predominately due to the increase in rain evaporation from the new cumulus parameterization. All-sky OLR biases agree well with the high-level CF comparisons. For example, both the P5- and C5-simulated upper-level CFs are ~11% higher than CERES observations, while both the P5- and C5-simulated all-sky OLRs are $\sim 2.5\,\mathrm{W\,m^{-2}}$ lower than observations within the UW regime due to high-level cloud tops having a much colder temperature than the sea surface. This argument is also true within the DW regime, where the C5-simulated high-level CF is 9.25% higher and all-sky OLR is $1.76\,\mathrm{W\,m^{-2}}$ lower than the CERES observations. P5 shows particularly good agreement in simulated high-level CF and all-sky OLR when compared with CERES observations within the defined DW regime. In general, the P5 simulation shows more improvement within the DW regime, where mean biases and RMSEs have decreased moderately compared to previous C5 results.

In Part I of this study, a quantitative comparison was performed to assess the improvement in the P5-simulated CF and cloud properties over the SMLs. To further investigate the impact of these improved cloud properties on the TOA radiation budget, we again focus on the SMLs using the data presented in Table 3 and Fig. 14. Through this comprehensive analysis, it is our hope that the modeling community may benefit from the modified PBL scheme implemented within the new GISS-E2 P5 GCM simulation, as many of the GCMs undersimulate MBL clouds over the SMLs when compared to the CERES observations (Dolinar et al. 2014).

As discussed in Part I of this study and presented here in Fig. 14, the P5-simulated total column CF increased ~12% over the SMLs compared to its C5 predecessor (Fig. 14a), largely as a result of the newly modified PBL scheme and the associated ~18% increase in low-level MBL clouds (Fig. 14b). This increase in total column CF from enhanced MBL clouds has outperformed the underestimation of CWP in the SMLs (Fig. 14c), resulting in a ~6% increase in all-sky albedo compared to the previous C5 simulation (Fig. 14e). While it does not make physical sense to have higher albedo with lower CF and CWP compared to the observations, this result may be partially explained by the ~20% increase in P5-simulated MBL clouds. Note that comparisons of MBL CF should be used with caution as passive satellites often cannot observe low-level clouds if there is an optically thick cloud layer above it. PWV and all-sky OLR comparisons (Figs. 14e,f) are similar to those in the defined DW regime, with slight improvements found in the P5 simulation. Minimal changes are observed in all-sky OLR fields over the SMLs (Fig. 14f), as there is no significant difference between MBL cloud-top temperature and SST. To summarize our findings over the SMLs, we list statistics of global means, standard deviations, biases in the global means, RMSE, and pattern correlations, calculated using annual-mean maps, for all cloud and radiation properties from the model simulations and observations, as well as their comparisons in Table 3. The largest improvements are found in the P5-simulated all-sky SW absorption, albedo, and SW CRE fields in response to the increase in MBL CF.

5. Summary and conclusions

In this study, the NASA GISS CMIP5 (C5)- and post-CMIP5 (P5)-simulated TOA radiation budgets and cloud radiative effects (CREs) were assessed utilizing the observed CERES EBAF (CE) satellite product, with a particular focus on large-scale atmospheric upwelling and downwelling regimes, the southern midlatitudes, and marine stratocumulus regions. Based on multiyear comparisons of the P5 and C5 versions of the GISS-E2 GCM against the CE observations, the following conclusions have been made.

1) Overall, the P5- and C5-simulated global patterns of clear-sky outgoing longwave radiation (OLR) match

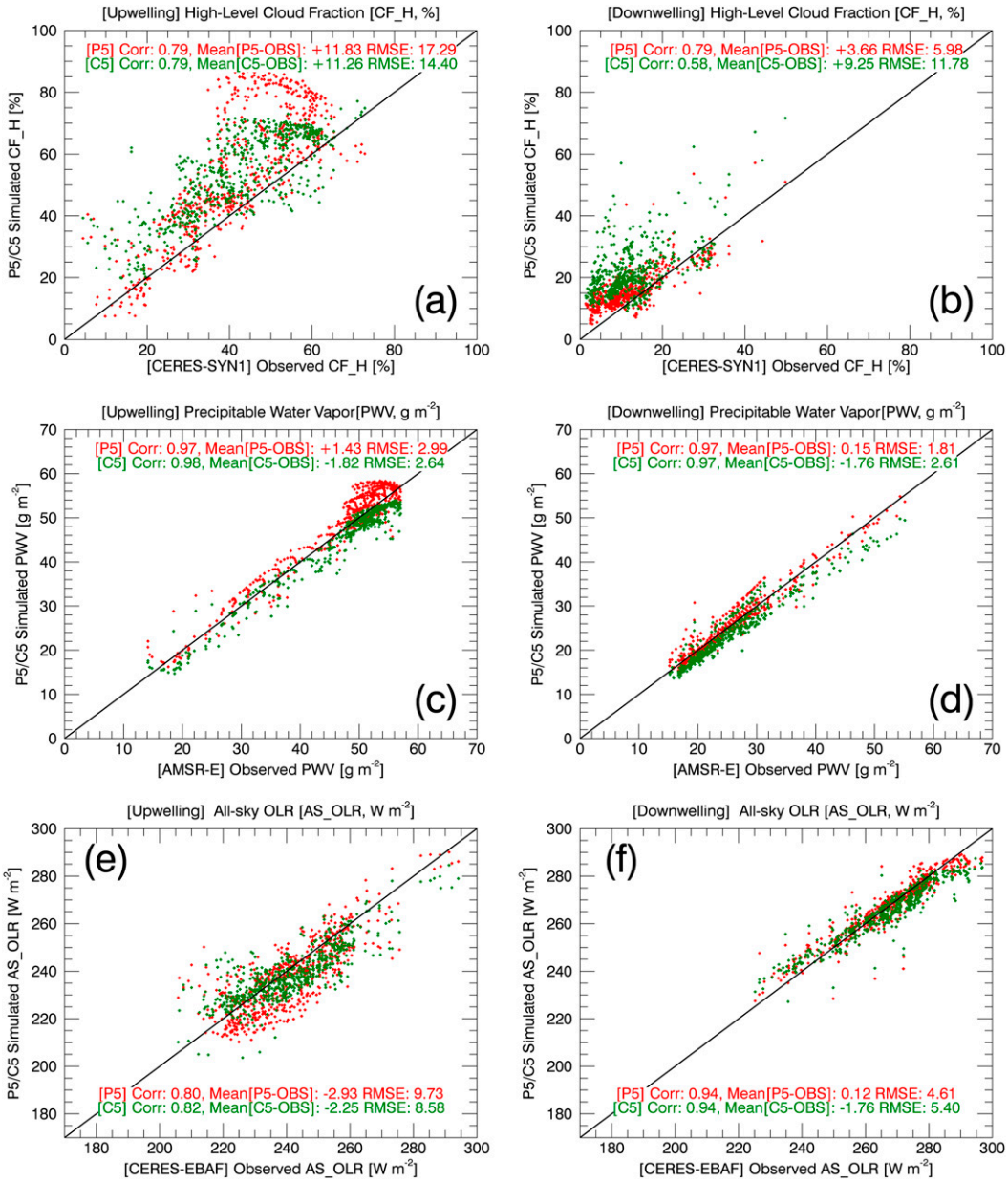

FIG. 13. As in Fig. 12, but for (a),(b) high-level cloud fraction (pressure < 440 hPa), (c),(d) precipitable water vapor, and (e),(f) all-sky OLR.

well with CE observations (Fig. 1). Global averages of the P5- and C5-simulated clear-sky OLR are ~4 and ~8 W m^{-2}, respectively, lower than the CE observation (266.1 W m^{-2}). These biases are partially due to the dry bias issue of comparing simulated clear-sky OLR with observations; however, this cannot explain the full bias found. Regional analysis of the biases in all-sky OLR revealed strong correlations to both PWV and total column CF. Further study has revealed that LW CREs also have strong correlations with PWV and total column CFs; thus, it is concluded that clouds and PWV play major roles in calculating LW CRE.

2) Global means of clear-sky and all-sky albedo were found to be nearly identical between all three datasets. On a regional scale, however, large biases are found in all-sky albedo (Fig. 4). As discussed in Part I, the MBL cloud fractions over the SMLs increased ~20% in the P5 simulation compared to its C5 predecessor, due to the implementation of the new PBL scheme. This increase in MBL CF over the SMLs has resulted in increased all-sky albedo and

TABLE 3. As in Table 2, but for the SMLs.

Variable	Dataset	Mean	Std dev	Bias	RMSE	Correlation	Quicklook
OLR (CLR-SKY) ($W\,m^{-2}$)	P5	253.3	15.19	−6.1	6.25	0.99	I, I, I, -
	C5	250.3	14.20	−9.1	9.06	0.99	
	CE	259.4	14.82	—	—	—	
OLR (ALL-SKY) ($W\,m^{-2}$)	P5	232.5	14.96	+3.3	4.69	0.99	I, I, I, -
	C5	232.6	14.34	+3.4	5.46	0.98	
	CE	229.2	16.83	—	—	—	
Albedo (CLR-SKY) (%)	P5	0.146	0.052	+0.007	0.045	0.84	W, I, W, W
	C5	0.151	0.040	+0.012	0.040	0.88	
	CE	0.139	0.031	—	—	—	
Albedo (ALL-SKY) (%)	P5	0.352	0.078	+0.008	0.034	0.97	W, I, I, I
	C5	0.306	0.061	−0.038	0.036	0.92	
	CE	0.344	0.067	—	—	—	
SW absorption (CLR-SKY) ($W\,m^{-2}$)	P5	271.3	39.83	−0.5	4.12	0.99	W, I, W, -
	C5	269.1	38.44	−2.7	3.78	0.99	
	CE	271.8	37.88	—	—	—	
SW absorption (ALL-SKY) ($W\,m^{-2}$)	P5	207.0	44.53	+0.4	5.57	0.99	I, I, I, I
	C5	220.4	40.75	+13.8	16.56	0.98	
	CE	206.6	43.71	—	—	—	
LW CRE ($W\,m^{-2}$)	P5	20.8	3.75	−9.4	10.02	0.78	I, I, I, I
	C5	17.8	3.63	−12.4	13.08	0.67	
	CE	30.2	4.49	—	—	—	
SW CRE ($W\,m^{-2}$)	P5	−64.3	12.06	+0.8	6.82	0.84	I, I, I, I
	C5	−48.6	7.71	+16.5	19.09	0.65	
	CE	−65.1	11.30	—	—	—	
Net CRE ($W\,m^{-2}$)	P5	−43.5	10.95	−8.6	10.84	0.80	I, W, W, I
	C5	−30.8	6.11	+4.1	8.15	0.70	
	CE	−34.9	9.57	—	—	—	

decreased SW absorption at TOA (Fig. 5) in the P5 simulation.

3) Analyses of spatial variability using the Taylor diagram showed large improvements in correlations of simulated SW and net CRE, with an insignificant sacrifice in variability. LW CRE correlations between the models and CE observations remained static; however, improvements were found in the LW CRE variability. P5–C5 correlation and variability comparisons continue to show good agreement with CE observations for all other variables, which is expected given the already high agreement found when comparing previous model simulations with CE observations.
4) To explore the regional differences between the model simulations and the observations, we define regions of large-scale vertical ascent–descent using vertical pressure velocity (ω) as a proxy. Regimes of strong atmospheric upwelling (UW; $\omega < -25\,\mathrm{hPa\,day^{-1}}$) and downwelling (DW; $\omega > 25\,\mathrm{hPa\ day^{-1}}$) are identified. Although the differences in all-sky albedo between the P5–C5 simulations and CERES observations in both regimes are small, they are not well correlated with the CF and CWP comparisons. PWV simulated by both P5 and C5 simulations have an excellent agreement with the AMSR-E observations, with nearly perfect pattern correlations over UW and DW regimes. All-sky OLR biases agree well with high-level CF comparisons. In general, the P5 simulation shows more improvement within the DW regime, where mean biases and RMSEs have decreased moderately compared to previous C5 results.

Overall, minimal changes were observed between the P5 and C5 simulations when looking at various fields during clear-sky scenes. With the adjustments to turbulence (Yao and Cheng 2012) and moist convection (Del Genio et al. 2012), large changes are, however, observed regionally during all-sky scenes. These changes come predominately in the form of improvements compared to CE observations, with particular attention to the SMLs. A second quantitative comparison over the SMLs was performed and has validated the improvements found in Part I of our study. Changes to low-level and total column CFs and cloud properties, resulting from changes to the P5 PBL parameterization, have shown great improvement across almost all radiative variables presented in Part II of this study. The strongest improvements in the SMLs have been found in SW fields during all-sky conditions, where increased CF

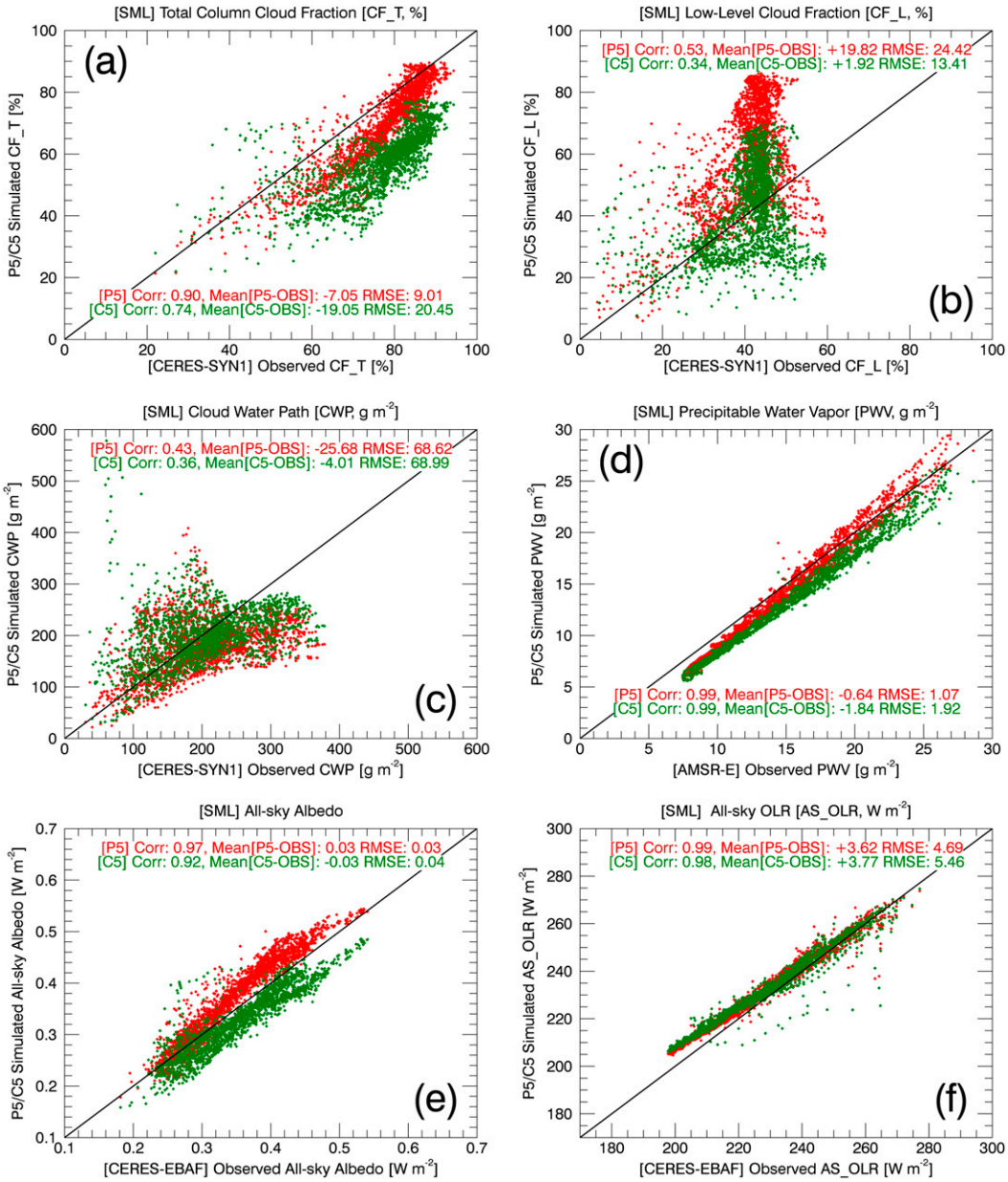

FIG. 14. Scatterplots of (a) total column cloud fraction CF, (b) low-level cloud fraction (pressure > 660 hPa), (c) cloud water path (CWP), (d) precipitable water vapor (PWV), (e) all-sky albedo, and (f) all-sky OLR over the SMLs (between 30° and 60°S).

in the P5 simulation has led to increased reflected shortwave and higher albedos.

Clear-sky OLR comparisons have raised questions for which we cannot yet answer at this time. A strengthening of the dry bias associated with comparing P5-simulated clear-sky OLR with CE observations was expected; however, the dry bias weakened in the presence of increased columnar PWV and decreased CWP. It is noted, however, that the possibilities of bias from the P5 and C5 simulations cannot be ruled out. Further research will be conducted to analyze what factors are contributing to the bias of P5-simulated clear-sky OLR under increased PWV conditions.

Acknowledgments. This work was supported by NASA EPSCoR CAN under Grant NNX11AM15A, NASA CERES project under Grant NNX10AI05G at the University of North Dakota, and by the NASA *CloudSat*/*CALIPSO* and Modeling and Analysis Program RTOPs at NASA/GISS. NASA GISS-E2

Post-CMIP5 GCM diagnostic run data are provided by NASA GISS directly. NASA GISS-E2 CMIP5 GCM data are provided by NASA GISS through the CMIP5 ESGF PCMDI database at http://pcmdi9.llnl.gov/esgf-web-fe/. The simulations were performed at the NASA Center for Climate Simulation at the Goddard Space Flight Center. CERES EBAF products used in this study are produced by the NASA CERES Team, available at http://ceres.larc.nasa.gov.

REFERENCES

Bony, S., and J.-L. Dufresne, 2005: Marine boundary layer clouds at the heart of tropical cloud feedback uncertainties in climate models. *Geophys. Res. Lett.,* **32,** L20806, doi:10.1029/2005GL023851.

——, and Coauthors, 2006: How well do we understand and evaluate climate change feedback processes? *J. Climate,* **19,** 3445–3482, doi:10.1175/JCLI3819.1.

Cess, R. D., and Coauthors, 1989: Interpretation of cloud–climate feedback as produced by 14 atmospheric general circulation models. *Science,* **245,** 513–516, doi:10.1126/science.245.4917.513.

Chen, L., Y. Yu, and D. Sun, 2013: Cloud and water vapor feedbacks to the El Niño warming: Are they still biased in CMIP5 models? *J. Climate,* **26,** 4947–4961, doi:10.1175/JCLI-D-12-00575.1.

Del Genio, A. D., Y.-H. Chen, D. Kim, and M.-S. Yao, 2012: The MJO transition from shallow to deep convection in *CloudSat/CALIPSO* data and GISS GCM simulations. *J. Climate,* **25,** 3755–3770, doi:10.1175/JCLI-D-11-00384.1.

Doelling, D. R., and Coauthors, 2013: Geostationary enhanced temporal interpolation for CERES flux products. *J. Atmos. Oceanic Technol.,* **30,** 1072–1090, doi:10.1175/JTECH-D-12-00136.1.

Dolinar, E., X. Dong, B. Xi, J. Jiang, and H. Su, 2014: Evaluation of CMIP5 simulated clouds and TOA radiation budgets using NASA satellite observations. *Climate Dyn.,* doi:10.1007/s00382-014-2158-9, in press.

Dong, X., and G. G. Mace, 2003: Arctic stratus cloud properties and radiative forcing derived from ground-based data collected at Barrow, Alaska. *J. Climate,* **16,** 445–461, doi:10.1175/1520-0442(2003)016<0445:ASCPAR>2.0.CO;2.

——, B. Xi, and P. Minnis, 2006: A climatology of midlatitude continental clouds from the ARM SGP central facility. Part II: Cloud fraction and surface radiative forcing. *J. Climate,* **19,** 1765–1783, doi:10.1175/JCLI3710.1.

——, and Coauthors, 2008: Using observations of deep convective systems to constrain atmospheric column absorption in the optically thick limit. *J. Geophys. Res.,* **113,** D10206, doi:10.1029/2007JD009769.

——, ——, K. Crosby, C. N. Long, R. Stone, and M. D. Shupe, 2010: A 10 year climatology of Arctic cloud fraction and radiative forcing at Barrow, Alaska. *J. Geophys. Res.,* **115,** D17212, doi:10.1029/2009JD013489.

——, ——, and P. Wu, 2014: Investigation of diurnal variation of MBL cloud microphysical properties at the Azores. *J. Climate,* **27,** 8827–8835, doi:10.1175/JCLI-D-14-00434.1.

Flato, G., and Coauthors, 2013: Evaluation of climate models. *Climate Change 2013: The Physical Science Basis,* T. F. Stocker et al., Eds., Cambridge University Press, 743–824 [Available online at http://www.ipcc.ch/pdf/assessment-report/ar5/wg1/WG1AR5_Chapter09_FINAL.pdf.]

Houghton, J. T., Y. Ding, D. J. Griggs, M. Noguer, P. J. van der Linden, X. Dai, K. Maskell, and C. A. Johnson, Eds., 2001: *Climate Change 2001: The Scientific Basis.* Cambridge University Press, 944 pp.

Jiang, J. H., and Coauthors, 2012: Evaluation of cloud and water vapor simulations in CMIP5 climate models using NASA "A-Train" satellite observations. *J. Geophys. Res.,* **117,** D14105, doi:10.1029/2011JD017237.

Kato, S., and N. G. Loeb, 2005: Top-of-atmosphere shortwave broadband observed radiance and estimated irradiance over polar regions from Clouds and the Earth's Radiant Energy System (CERES) instruments on *Terra. J. Geophys. Res.,* **110,** D07202, doi:10.1029/2004JD005308.

——, ——, F. G. Rose, D. R. Doelling, D. A. Rutan, T. E. Caldwell, L. Yu, and R. A. Weller, 2013: Surface irradiances consistent with CERES-derived top-of-atmosphere shortwave and longwave irradiances. *J. Climate,* **26,** 2719–2740, doi:10.1175/JCLI-D-12-00436.1.

Kim, D., A. H. Sobel, A. D. Del Genio, Y. Chen, S. J. Camargo, M.-S. Yao, M. Kelley, and L. Nazarenko, 2012: The tropical subseasonal variability simulated in the NASA GISS general circulation model. *J. Climate,* **25,** 4641–4659, doi:10.1175/JCLI-D-11-00447.1.

Klein, S. A., Y. Zhang, M. D. Zelinka, R. Pincus, J. Boyle, and P. J. Gleckler, 2013: Are climate model simulations of clouds improving? An evaluation using the ISCCP simulator. *J. Geophys. Res. Atmos.,* **118,** 1329–1342, doi:10.1002/jgrd.50141.

Kopp, G., and G. Lawrence, 2005: The Total Irradiance Monitor (TIM): Instrument design. *Sol. Phys.,* **230,** 91–109, doi:10.1007/s11207-005-7446-4.

Lauer, A., and K. Hamilton, 2013: Simulating clouds with global climate models: A comparison on CMIP5 results with CMIP3 and satellite data. *J. Climate,* **26,** 3823–3845, doi:10.1175/JCLI-D-12-00451.1.

Li, J.-L. F., D. E. Waliser, G. Stephens, S. Lee, T. L'Ecuyer, S. Kato, N. Loeb, and H.-Y. Ma, 2013: Characterizing and understanding radiation budget biases in CMIP3/CMIP5 GCMs, contemporary GCM, and reanalysis. *J. Geophys. Res. Atmos.,* **118,** 8166–8184, doi:10.1002/jgrd.50378.

Loeb, N. G., K. J. Priestley, D. P. Kratz, E. B. Geier, R. N. Green, B. A. Wielicki, P. O. Hinton, and S. K. Nolan, 2001: Determination of unfiltered radiances from the Clouds and the Earth's Radiant Energy System (CERES) instrument. *J. Appl. Meteor.,* **40,** 822–835, doi:10.1175/1520-0450(2001)040<0822:DOURFT>2.0.CO;2.

——, N. Manalo-Smith, S. Kato, W. F. Miller, S. K. Gupta, P. Minnis, and B. A. Wielicki, 2003: Angular distribution models for top-of-atmosphere radiative flux estimation from the Clouds and the Earth's Radiant Energy System instrument on the Tropical Rainfall Measuring Mission Satellite. Part I: Methodology. *J. Appl. Meteor.,* **42,** 240–265, doi:10.1175/1520-0450(2003)042<0240:ADMFTO>2.0.CO;2.

——, S. Kato, K. Loukachine, and N. M. Smith, 2005: Angular distribution models for top-of-atmosphere radiative flux estimation from the Clouds and the Earth's Radiant Energy System instrument on the *Terra* satellite. Part I: Methodology. J. *Atmos. Oceanic Technol.,* **22,** 338–351, doi:10.1175/JTECH1712.1.

——, W. Sun, W. F. Miller, K. Loukachine, and R. Davies, 2006: Fusion of CERES, MISR, and MODIS measurements for

top-of-atmosphere radiative flux validation. *J. Geophys. Res.,* **111,** D18209, doi:10.1029/2006JD007146.

——, and Coauthors, 2007: Multi-instrument comparison of top-of-atmosphere reflected solar radiation. *J. Climate,* **20,** 575–591, doi:10.1175/JCLI4018.1.

——, B. A. Wielicki, D. R. Doelling, G. L. Smith, D. F. Keyes, S. Kato, N. Manalo-Smith, and T. Wong, 2009: Toward optimal closure of the Earth's top-of-atmosphere radiation budget. *J. Climate,* **22,** 748–766, doi:10.1175/2008JCLI2637.1.

——, S. Kato, W. Su, T. Wong, F. G. Rose, D. R. Doelling, J. R. Norris, and X. Huang, 2012a: Advances in understanding top-of-atmosphere radiation variability from satellite observations. *Surv. Geophys.,* **33,** 359–385, doi:10.1007/s10712-012-9175-1.

——, J. M. Lyman, G. C. Johnson, R. P. Allan, D. R. Doelling, T. Wong, B. J. Soden, and G. L. Stephens, 2012b: Observed changes in top-of-the-atmosphere radiation and upper-ocean heating consistent within uncertainty. *Nat. Geosci.,* **5,** 110–113, doi:10.1038/NGEO1375.

Minnis, P., and Coauthors, 2011a: CERES edition-2 cloud property retrievals using TRMM VIRS and *Terra* and *Aqua* MODIS Data—Part I: Algorithms. *IEEE Trans. Geosci. Remote Sens.,* **49,** 4374–4400, doi:10.1109/TGRS.2011.2144601.

——, and Coauthors, 2011b: CERES edition-2 cloud property retrievals using TRMM VIRS and *Terra* and *Aqua* MODIS data—Part II: Examples of average results and comparisons with other data. *IEEE Trans. Geosci. Remote Sens.,* **49,** 4401–4430, doi:10.1109/TGRS.2011.2144602.

Ramanathan, V., R. D. Cess, E. F. Harrison, P. Minnis, B. R. Barkstrom, E. Ahmad, and D. Hartmann, 1989: Cloud-radiative forcing and climate: Results from the Earth Radiation Budget Experiment. *Science,* **243,** 57–63, doi:10.1126/science.243.4887.57.

Randall, D. A., and Coauthors, 2007: Climate models and their evaluation. *Climate Change 2007: The Physical Science Basis,* S. Solomon et al., Eds., Cambridge University Press, 589–662.

Schmidt, G. A., and Coauthors, 2014: Configuration and assessment of the GISS ModelE2 contributions to the CMIP5 archive. *J. Adv. Model. Earth Syst.,* **6,** 141–184, doi:10.1002/2013MS000265.

Sohn, B., and R. Bennartz, 2008: Contribution of water vapor to observational estimates of longwave cloud radiative forcing. *J. Geophys. Res.,* **113,** D20107, doi:10.1029/2008JD010053.

——, J. Schmetz, R. Stuhlmann, and J. Lee, 2006: Dry bias in satellite-derived clear-sky water vapor and its contribution to longwave cloud radiative forcing. *J. Climate,* **19,** 5570–5580, doi:10.1175/JCLI3948.1.

Stanfield, R., X. Dong, B. Xi, A. Kennedy, A. D. Del Genio, P. Minnis, and J. Jiang, 2014: Assessment of NASA GISS CMIP5 and post-CMIP5 simulated clouds and TOA radiation budgets using satellite observations. Part I: Cloud fraction and properties. *J. Climate,* **27,** 4189–4208, doi:10.1175/JCLI-D-13-00558.1.

Stephens, G. L., 2005: Cloud feedbacks in the climate system: A critical review. *J. Climate,* **18,** 237–273, doi:10.1175/JCLI-3243.1.

Su, H., and Coauthors, 2013: Diagnosis of regime-dependent cloud simulation errors in CMIP5 models using "A-Train" satellite observations and reanalysis data. *J. Geophys. Res.,* **118,** 2762–2780, doi:10.1029/2012JD018575.

Taylor, K. E., 2001: Summarizing multiple aspects of model performance in a single diagram. *J. Geophys. Res.,* **106** (D7), 7183–7192, doi:10.1029/2000JD900719.

——, R. J. Stouffer, and G. A. Meehl, 2012: An overview of CMIP5 and the experiment design. *Bull. Amer. Meteor. Soc.,* **93,** 485–498, doi:10.1175/BAMS-D-11-00094.1.

Wang, H., and W. Su, 2013: Evaluating and understanding top of the atmosphere cloud radiative effects in International Panel on Climate Change (IPCC) AR5 CMIP5 models using satellite observations. *J. Geophys. Res. Atmos.,* **118,** 683–699, doi:10.1029/2012JD018619.

Wielicki, B. A., R. D. Cess, M. D. King, D. A. Randall, and E. F. Harrison, 1995: Mission to planet Earth: Role of clouds and radiation in climate. *Bull. Amer. Meteor. Soc.,* **76,** 2125–2153, doi:10.1175/1520-0477(1995)076<2125:MTPERO>2.0.CO;2.

——, B. R. Barkstrom, E. F. Harrison, R. B. Lee III, G. L. Smith, and J. E. Cooper, 1996: Clouds and the Earth's Radiant Energy System (CERES): An Earth observing system experiment. *Bull. Amer. Meteor. Soc.,* **77,** 853–868, doi:10.1175/1520-0477(1996)077<0853:CATERE>2.0.CO;2.

Yao, M.-S., and Y. Cheng, 2012: Cloud simulations in response to turbulence parameterizations in the GISS Model E GCM. *J. Climate,* **25,** 4963–4974, doi:10.1175/JCLI-D-11-00399.1.

Young, D. F., P. Minnis, D. R. Doelling, G. G. Gibson, and T. Wong, 1998: Temporal interpolation methods for the Clouds and Earth's Radiant Energy System (CERES) Experiment. *J. Appl. Meteor.,* **37,** 572–590, doi:10.1175/1520-0450(1998)037<0572:TIMFTC>2.0.CO;2.